

U-Pb ГЕОХРОНОЛОГИЯ ЦИРКОНА И Hf-ИЗОТОПНЫЕ И ПЕТРОХИМИЧЕСКИЕ ХАРАКТЕРИСТИКИ ПАЛЕОЦЕНОВЫХ ГРАНИТОИДОВ ЗАПАДНОЙ ЧАСТИ ПОЯСА ГАНГДЕЗЕ (Тибет)

Ц. Линь^{1,3}, Ф. Дин^{1,2}, Ц. Чэн^{1,2}, Т. Шень³

¹College of Earth Sciences, Chengdu University of Technology, Chengdu Sichuan, 610059, China

²Key Laboratory of Tectonic Controls on Mineralization and Hydrocarbon Accumulation, Ministry of Natural Resources, Chengdu University of Technology, Chengdu Sichuan, 610059, China

³403 Geological Brigade of Sichuan Bureau of Geology and Mineral Resources, Emei, 614200, China

Группа исследователей изучила петрологический и валовый геохимический состав, U-Pb возраст циркона и характеристики стабильных изотопов гранитов Жунголунба и Гажунцо в районе Ноцан для уточнения влияния субдукции океана Нео-Тетис и столкновения Индийского и Евразийского континентов на тектономагматические процессы, протекавшие в палеоцене вдоль южной окраины пояса Гангдезе. Гранит Жунголунба и гранит-порфир Гажунцо образовались 61.86 млн лет и 62.17 млн лет назад соответственно. Гранитоиды района Ноцан характеризуются: 1) высоким содержанием SiO_2 , NaO_2 и Al_2O_3 и низким содержанием $\text{FeO}_{\text{общ}}$, MgO и TiO_2 ; 2) обогащенностью лёгкими редкоземельными и крупноионными лиофильными элементами и обедненностью тяжёлыми редкоземельными и высокозарядными элементами (Nb , P и Ti); 3) выраженным отрицательным европиевым аномалиям. Эти особенности указывают на то, что граниты района Ноцан относятся к высококалиевому известково-щелочному и высокоглиноземистому типам. Кроме того, изотопные характеристики Hf в цирконах гранитов указывают на древний кристаллический фундамент области их магматического источника. Андезитобазальтовый кристаллический туф является продуктом частичного плавления гранатового перидотита и контаминации земной коры в результате внедрения восходящей магмы.

U-Pb датирование циркона, изотоп Hf, район Ноцан, Пояс Гангдезе

ZIRCON U-Pb GEOCHRONOLOGY, Hf ISOTOPE COMPOSITION, AND PETROCHEMICAL CHARACTERISTICS OF PALEOCENE GRANITOIDS IN THE WESTERN GANGDESE BELT, TIBET

J.Q. Lin, F. Ding, C.H. Chen, T. Shen

The research team studied the petrology, whole-rock geochemistry, zircon U-Pb age, and stable isotopic characteristics of the Rongguo Longba and Garongcuo granites of the Nuocang area to understand better the impact of Neo-Tethys ocean subduction and India-Eurasia continental collision on Paleocene tectonomagmatic processes along the southern margin of the Gangdese Belt. The Rongguo Longba granite and Garongcuo granite porphyry formed at 61.86 and 62.17 Ma, respectively. The Nuocang granitoids are characterized by (1) high SiO_2 , NaO_2 , and Al_2O_3 contents and low FeO_{tot} , MgO , and TiO_2 contents; (2) LREE and LILE enrichment and HREE and HFSE (Nb , P , and Ti) depletion; and (3) obvious negative Eu anomalies. These features indicate that the Nuocang granites are of the high-K calc-alkaline and peraluminous granite types. Furthermore, their zircon Hf isotope characteristics suggest that the magma source region has an ancient crystalline basement. The basaltic andesitic crystal tuff is the product of garnet-peridotite partial melting and crust contamination from rising magma emplacement.

Zircon U-Pb dating, Hf isotope, Nuocang area, Gangdese Belt

INTRODUCTION

The timing and process of the Indian-Eurasian continental collision is the most important scientific issue in the Qinghai-Tibet Plateau research. Geologists are understandably concerned with this crucial event, as the plate collision came to control the global tectonic framework, Asian landforms, circulation of the surrounding ocean, biogenetic derivation, and global climate change (Wang and Ding, 2003). The Gangdese Belt (Lhasa Block) is a massive magmatic tectonic belt located between the Yarlung Zangbo Suture Zone (YZSZ) and the Bangong-Nujiang Suture Zone (BNSZ), spanning about 2000 km east to west and 80 km north to south. Over

80% of the entire Qinghai–Tibet Plateau magma distribution area is found in the Gangdese Belt. These igneous rocks give an insight into the tectonic evolution and deep Gangdese Belt processes, serving as a “probe” and “window” to the Tethys Ocean subduction and continental collision dynamics (Chung et al., 2003; Mo et al., 2005, 2009; Pan et al., 2006; Hou et al., 2008; Ji et al., 2009a,b; Xu, 2010; Zhu et al., 2011, 2015; Zhang et al., 2013, 2017; Tang et al., 2015; Wang et al., 2015; Sun et al., 2017; Stupak et al., 2020). Researchers have ascertained—based on the paleomagnetics, paleontology, tectonics, sedimentary petrology, magmatic petrology, and metamorphic petrology data—that the time interval of the initial collision between the Indian and Eurasian continents is limited to 70–34 Ma (Garzanti et al., 1987; Searle et al., 1987; Dewey, 1989; Rowley, 1996; Yin and Harrison, 2000). Hou et al. (2008) further restrict this window to 65 Ma, according to regional petrology, isotope chronology, and paleogeographical evidence. Thus, Paleocene–Eocene granites are highly significant to our understanding of this continental collision process. Collision-related volcanic rocks, intrusions, and dikes are distributed largely across the Gangdese Belt. The intrusive rocks occur as a series of small granite batholiths and intermediate–basic dikes. However, the volcanic rocks belong to the Late Cretaceous–Eocene Linzizong Group, which can be further divided into the Dianzhong, Nianbo, and Pana Formations (from bottom to top). Volcanic strata are widely distributed across the southern Gangdese Belt. The diagenetic ages of the Dianzhong, Nianbo, and Pana Formations range from 68.7 to 59 Ma, from 56 to 52 Ma, and from 52 to 48 Ma, respectively (Jiang et al., 2018). The Linzizong Group in the eastern and western Gangdese Belt has a similar diagenetic age, but differs in rock type and composition. The Nianbo and Pana Formations are relatively developed in the western Gangdese Belt (Yu et al., 2010; Xie et al., 2013a; Bao et al., 2014; Dong et al., 2015). The Linzizong volcanic rocks are the product of the India–Eurasia collision. A regional unconformity corresponding to the proposed collision date of 65 Ma exists between the Linzizong Group volcanic rocks and lower strata, thus possibly marking the continental collision event. The Linzizong Group volcanic rocks may therefore represent the thickening of the southern Lhasa Block continental crust during the subduction of the Tethys oceanic crust and transition to collision (Mo and Pan, 2006; Wang et al., 2006; Mo et al., 2008, 2009; Dong et al., 2015; Lü et al., 2015).

Theoretical research on the Gangdese Belt Linzizong volcanic rocks has intensified in recent years, and interest in contemporaneous intrusions has grown. For example, granite porphyry at the western margin of the Linzhou Basin with a SHRIMP age of 58.7 Ma was interpreted as the result of partial melting caused by crustal shortening and heating during early-stage collision between India and Eurasia starting at about 65 Ma (Wang et al., 2006). Meanwhile, a study by Liu et al. (2018) finds, by petrogeochemical and isotopic dating, that the zircon U–Pb age of granites in the eastern Gangdese batholith is 57.6–68.7 Ma, indicating the same provenance with different ratios of crust to mantle (Liu et al., 2019). Wang et al. (2017) believe that the Riduo granite and granodiorite dikes with zircon U–Pb ages of 62.7–59.5 Ma formed by the partial melting of basic lower-crust materials against a background of continuous northward subduction of the New Tethyan Ocean. The above-referenced studies focus mainly on the eastern Gangdese Belt, while there has been little research conducted on the western Gangdese Belt Paleocene granite. The Nuocang area granitic bodies of the western Gangdese Belt are mainly granite and granite porphyry. In this paper, we present the zircon U–Pb chronology, whole-rock geochemical analysis, and zircon Hf isotope analysis of this granite. In combination with regional geological data, we aim to explain the characteristics of the India–Eurasia collision along with the age, provenance, and genesis of the Gangdese Belt granitoids.

GEOLOGIC BACKGROUND

The Qinghai–Tibet Plateau is separated by the Jinshajiang, Bangonghu–Nujiang, and Yarlungzangbo Suture Zones (JSSZ, BNSZ, and YZSZ, respectively) with an E–W trend into the Songpan–Ganzi, Qiangtang, Lhasa, and Himalaya Terranes from north to south (Li, 1987; Yin and Harrison, 2000; Pan et al., 2006; Xu et al., 2010; Zhang et al., 2017; Liu et al., 2018, 2019) (Fig. 1b). By its basement properties, the Lhasa Terrane (Gangdese Belt) can also be separated from north to south by the Shiquanhe–Namu Tso ophiolite mélange fault (SNMF) and the Luobadui–Milashan Fault (LMF) into the North, Central, and South Lhasa (NL, CL, and SL, respectively) Terranes (Zhu et al., 2009, 2011, 2013).

In the North Lhasa Terrane, large-scale Jurassic–Cretaceous igneous rocks developed, possibly with the southward subduction of the Bangonghu–Nujiang Ocean lithosphere and slab breakoff following collision with the Qiangtang Terrane (Mo et al., 2005; Pan et al., 2006; Zhu et al., 2009, 2013; Zhang et al., 2010–2012; Yan et al., 2017). The Precambrian basement of the Central Lhasa Terrane crystalline basement is currently identified as the Neoproterozoic Nianqingtanggula Group as found on the western bank of Namu Tso (Zhang et al., 2010; Dong et al., 2011). Its sedimentary cover is an Ordovician–Cenozoic volcanic sedimentary sequence with Permian–Eocene magmatic developments related to the opening, subduction, and closure of the Tethys Ocean in conjunction with the breakup and collision of different terranes (Pan et al., 2006; Zhu et al., 2011, 2013). The South Lhasa Terrane is characterized by large-scale distribution of Meso-Cenozoic igneous rocks, including the

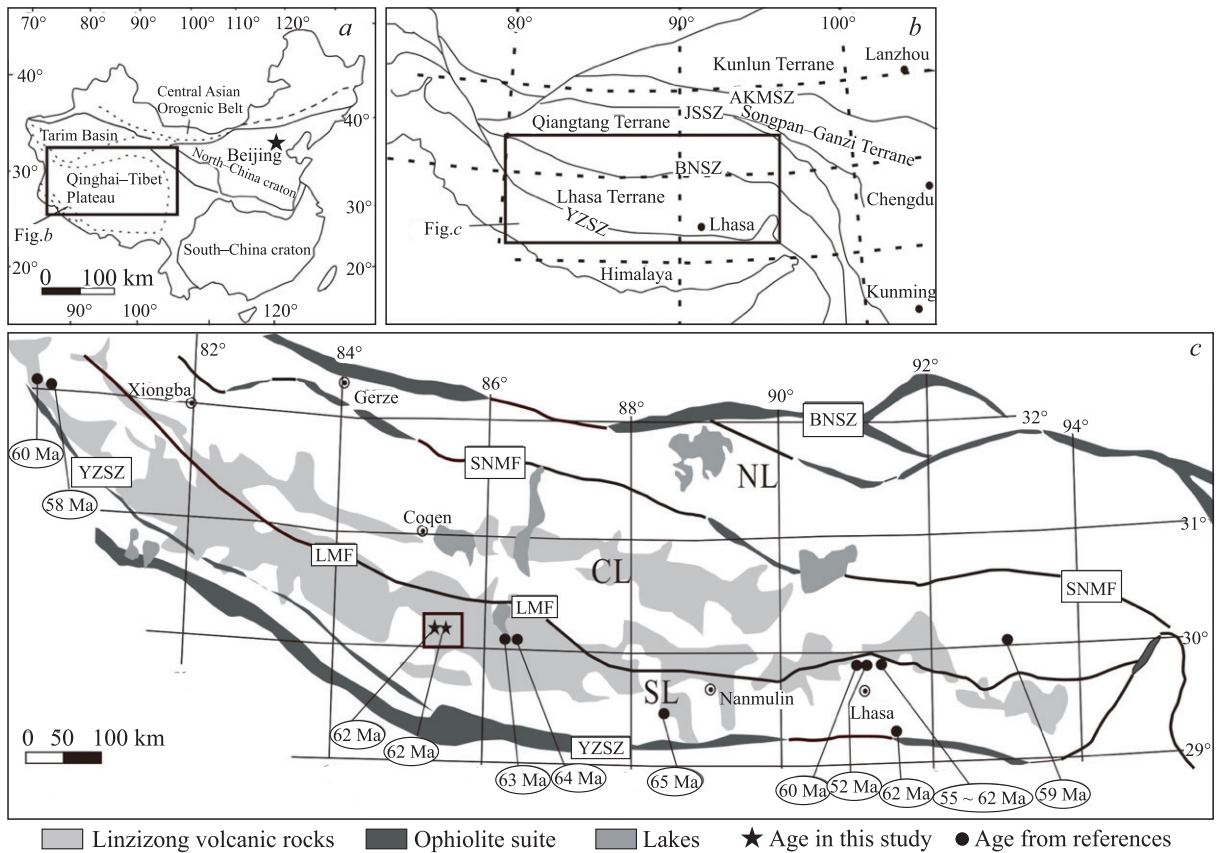


Fig. 1. Tectonic sketch map of China (after Zheng et al. (2014) (a); b, tectonic sketch map of the Qinghai-Tibet Plateau; c, simplified tectonic units of the Lhasa Terrane (after (Zhu et al., 2013)). The references to age data sources are the same as in Table 4.

famous Gangdese batholith and Linzizong volcanic rocks, as well as minor Triassic–Cretaceous volcanic–sedimentary rocks (Zhu et al., 2011, 2013; Zhang et al., 2013). At present, Hf isotope mapping shows the Lhasa Terrane NL and SL are dominated by juvenile crustal materials, while its CL is characterized by ancient crust (Zhang et al., 2013; Zhu et al., 2013).

The study area is located at the southern margin of the Gangdese Belt Coqen Basin, adjacent to the junction of the Central and South Lhasa Terranes (Fig. 1c). Here, the mainly developed sedimentary strata include (1) the Late Cretaceous–Eocene Linzizong volcanic succession and the Carboniferous–Permian metasedimentary series (Yongzhu, Laga, and Angjie formations). The Linzizong volcanic rocks create an unconformity with the Carboniferous–Permian metasedimentary series below. The Linzizong volcanic rocks only developed the Dianzhong and Nianbo formations in this area, which are of the calc-alkaline series. The Dianzhong Formation is composed of clastic crystalline tuff and a small amount of basalt. The Nianbo Formation is composed of gray-green rhyolitic tuff, rhyolite, and dacite, volcanic breccia, sandstone, and conglomerate (Bao et al., 2014; Ding et al., 2017) (Fig. 2).

GEOLOGY OF THE NUOCANG GRANITOID

The Paleocene Rongguo Longba granite composition is 50% plagioclase, 20–30% quartz, and 10–15% orthoclase, chlorite, and biotite. Accessory minerals include opaque minerals, such as apatite and zircon. Some granite shows sericitization, clayization, and chloritization (Fig. 3b).

The Garongcuo granite porphyry has a porphyritic texture (Fig. 3c). Phenocrysts account for about 35% of the volume, of which biotite, plagioclase, potassium feldspar, and quartz account for 5, 10, 15, and 5%, respectively. Plagioclase, potassium feldspar, and quartz particle sizes range from 0.3 to 1.0 mm, from 0.2 to 2.3 mm, and from 0.3 to 2 mm, respectively. The Garongcuo granite porphyry is 65% matrix, which is composed of plagioclase, potassium feldspar, and quartz, with particle sizes under 0.1 mm.

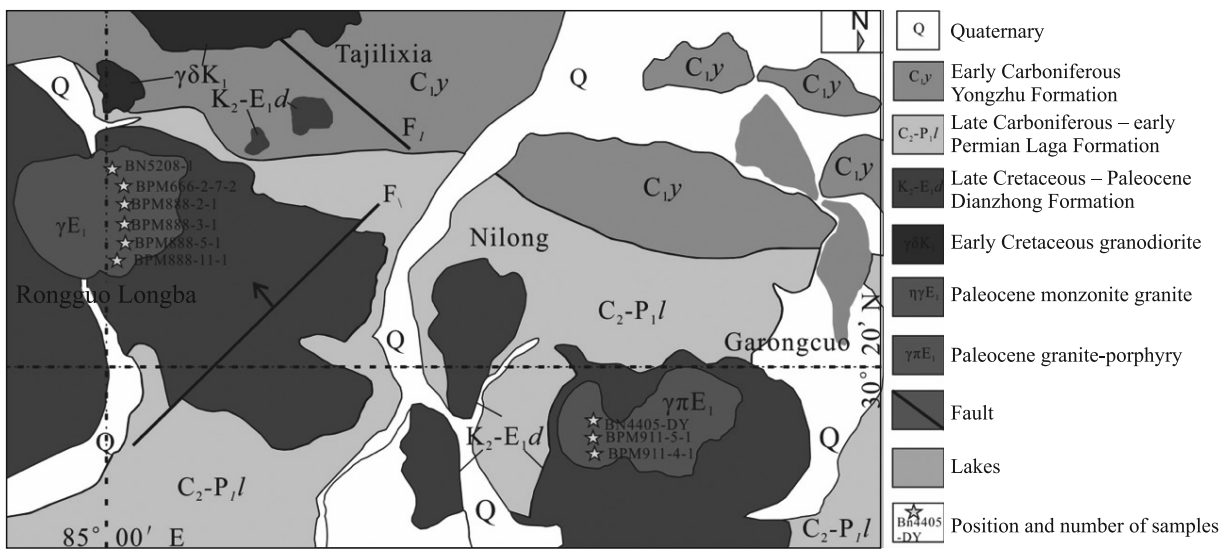


Fig. 2. Geological map of the study area.

Methodology

The samples in this study were bedrock with weak surface weathering. Weathered surface layers were removed from samples before analysis. The agate mortar was cleaned with chemical ethanol in advance to prevent sample contamination. Zircon target and cathodoluminescence (CL) microphotography were conducted in

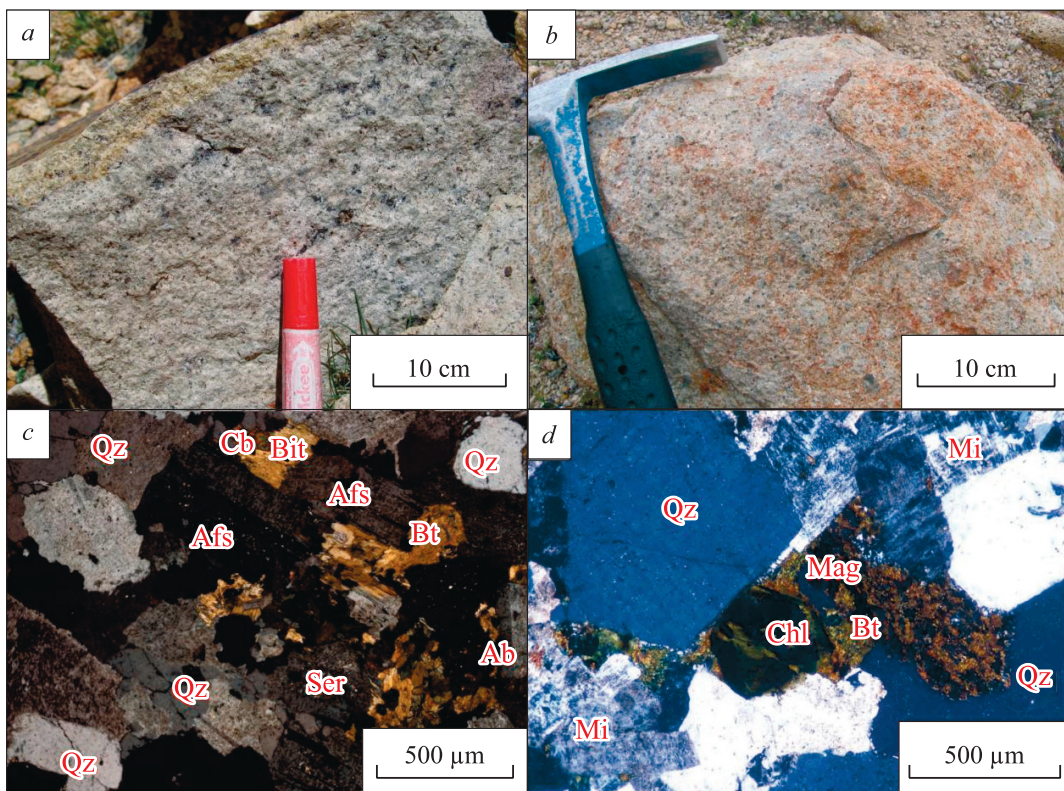


Fig. 3. The outcrops of the Guoluolongba granite in the Nuocang area, Tibet (a); the outcrops of the Garongcuo granite porphyry in the Nuocang area, Tibet (b); photomicrograph of granite (c); photomicrograph of granite (d).

Qz, quartz; Or, orthoclase feldspar; Cb, carbonate mineral; Bt, biotite; Mi, mica; Ser, sericite; Afs, Alkali feldspar; Ab, albite; Mag, magnetite; Chl, chlorite.

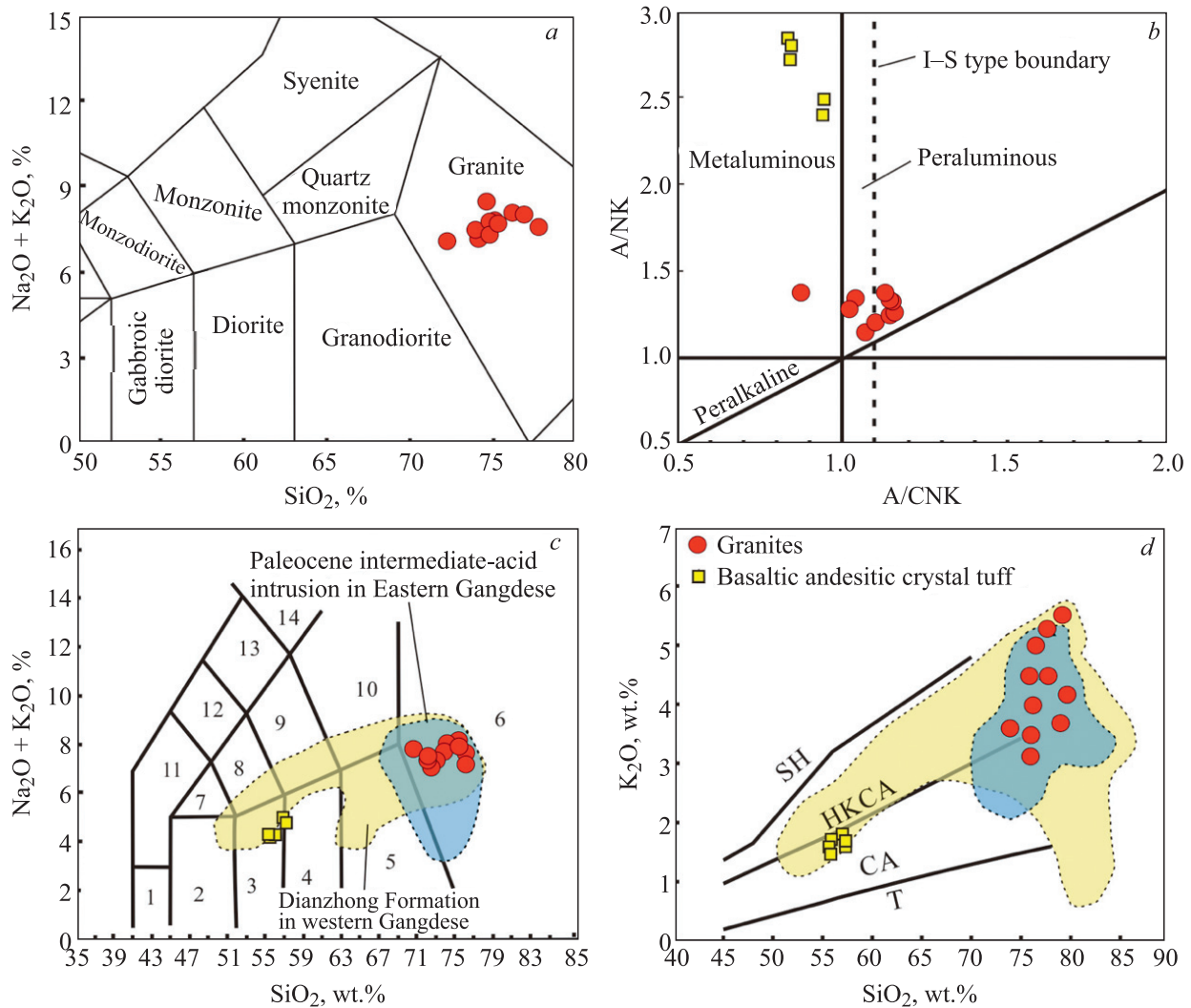


Fig. 4. Total alkali vs. silica (a) (Wilson, 2001); A/NK vs. A/CNK (b); total alkali vs. silica (TAS) (c); total alkali vs. silica (Le Maitre, 2002); K₂O–SiO₂ plot (d) (Rickwood, 1989). The data on the Nuocong area Linzizong Dianzhong Formation are as in (Hu, 2007; Bao, 2014; Jiang, 2018); the Eastern Gangdese Belt intrusion data are as in (Wang et al., 2006, 2019; Li et al., 2012; Dong et al., 2015).

1, picrite-basalt; 2, basalt; 3, basalt–andesite; 4, andesite; 5, dacite; 6, rhyolite; 7, trachybasalt; 8, basaltic trachyandesite; 9, amygdaloidal andesite; 10, trachyte; 11, tephrite; 12, phonolitic tephrite; 13, tephritic phonolite; 14, phonolite.

the laboratories of Beijing Zhongke Mine Research and Testing Technology Co., Ltd. The specific preparation process is described in detail by Song (2015). Zircon U–Pb isotope dating was conducted with the Agilent 7500a ICP MS at the State Key Laboratory of Geochemistry of Deposits, Institute of Geochemistry, Chinese Academy of Sciences. The laser beam diameter was 30 µm. Standard zircon 91500 (1064 Ma) (Wiedenbeck et al., 1995) and GJ-1 (600 Ma) served as external standards, and NISTSRM610 ²⁹Si was used as the internal standard. The error standard in the test was 1σ. The analysis data were processed by ICP MS DataCal 9.2.

A zircon Hf isotope test was conducted with Neptune plus multireceiver plasma mass spectrometry (MC ICP MS) and an NWR213nm solid-state laser in the Beijing Zhongke Mine Research and Testing Technology Co., Ltd. laboratory. During the experiment, helium was used to carry the denudation material, and the denudation diameter was 55 µm. GJ-1 and Plešovice zircon served as reference materials. The analysis point was in the same position as the U–Pb dating analysis point. The detailed analytical procedures and operating conditions were similar to those described by Hou et al. (2007). The weighted average values of ¹⁷⁶Hf/¹⁷⁷Hf of zircon standard GJ-1 were 0.282007 ± 0.000007 (2σ, n = 36), completely consistent with those reported in (Hou et al., 2007).

Samples were ground to 200 mesh and sent to the Southwest Metallurgical Geological Testing Institute of the Sichuan Province for chemical analysis. Major-element analysis was carried out using a PHILIPS PW 2404

Table 1. Major- (wt.%) and trace-element (ppm) contents of representative granite and granite porphyry samples

Sample	BN5208-1	BPM666-2-7-2	BPM888-2-1	BPM888-3-1	BPM888-5-1	BPM888-11-1	BPM911-4-1	BPM911-5-1	BN4405-DY	BPM911-6-1	BPM911-12-1
Component	1	2	3	4	5	6	7	8	9	10	11
SiO ₂	74.87	73.58	75.81	77.11	73.5	73.71	70.47	72.63	76.08	72.97	73.28
TiO ₂	0.14	0.19	0.1	0.09	0.18	0.18	0.24	0.23	0.13	0.23	0.19
Al ₂ O ₃	12.81	13.13	12.36	12.42	13.01	13.04	12.96	13.25	12.34	13.41	13.07
Fe ₂ O ₃	0.42	0.33	0.76	0.52	0.98	0.77	1.78	1.29	0.58	1.27	1.78
FeO	1.74	1.79	1.17	0.99	1.91	1.55	1.68	2.19	1.47	2.03	0.89
MnO	0.03	0.07	0.02	0.04	0.04	0.04	0.05	0.06	0.03	0.04	0.04
MgO	0.17	0.22	0.06	0.06	0.17	0.17	0.23	0.24	0.1	0.19	0.09
CaO	0.47	0.88	0.34	0.42	1.54	1.4	2.96	0.85	0.28	1.02	0.62
Na ₂ O	2.76	3.08	2.64	3.42	3.36	3.31	3.48	3.8	4.15	4.06	3.3
K ₂ O	5.21	4.38	5.38	4.14	3.93	4.39	3.43	3.47	3.67	3.02	4.93
P ₂ O ₅	0.03	0.04	0.01	0.01	0.04	0.04	0.06	0.06	0.02	0.06	0.04
LOI	1.35	2.31	1.36	0.78	1.35	1.41	2.68	1.93	1.15	1.69	1.83
Total	100.00	100.00	100.01	100.00	100.01	100.01	100.02	100.00	100.00	99.99	100.06
Rb	251.2	154.9	187.3	154.6	157.6	164.3	125.3	125.1	145.55	118.2	159.7
Sr	107.3	129.9	53.86	50	128.4	113.8	183.2	137.1	80.17	155.1	152
Y	14.3	33.75	43.79	43.86	37.79	38.9	35.56	36.31	36.91	32.86	28.04
Zr	104.78	176.72	145.1	141.67	172.16	183.29	199.46	186.22	183.35	217.46	168.06
Nb	6.83	9.15	9.33	7.71	10.08	9.94	12.26	7.54	10.09	11.4	7.28
Ba	547.9	540.3	314.3	311.45	530.3	429.1	587.2	636.1	643.25	658.4	794.2
La	37.9	49.68	48.53	35.36	48.03	38.68	52.48	59.55	41.46	59.21	58.4
Ce	71.76	82.1	96.05	86.92	94.48	78.57	101.72	108.35	74.19	110.27	108.39
Pr	7.77	10.56	11.39	10.16	13.31	12.55	13.48	15.42	9.42	12.71	13.93
Nd	30.14	41.31	44.59	39.37	54.2	48.86	54.41	59.77	40.11	51.2	52.74
Sm	4.46	7.11	8.82	8.45	10.61	9.57	10.19	10.64	7.53	9.08	8.95
Eu	0.73	0.99	0.59	0.57	1.42	1.12	1.92	1.8	1.18	1.72	1.62
Gd	3.84	6.64	8.27	7.72	10.21	9	9.41	9.52	7.14	8.23	9.03
Tb	0.51	1.03	1.4	1.32	1.63	1.35	1.39	1.37	1.15	1.18	1.28
Dy	2.55	5.88	8.27	7.86	9.33	7.66	7.66	7.48	6.61	6.49	7.1
Ho	0.5	1.18	1.76	1.71	1.92	1.59	1.6	1.48	1.35	1.32	1.42
Er	1.54	3.55	5.11	5.27	5.17	4.79	4.61	4.21	3.95	3.73	4.08
Tm	0.22	0.52	0.75	0.81	0.75	0.67	0.7	0.6	0.59	0.54	0.59
Yb	1.52	3.54	5.14	5.51	5.02	4.47	4.87	3.93	3.87	3.56	3.95
Lu	0.25	0.53	0.78	0.85	0.75	0.68	0.78	0.61	0.6	0.55	0.62
Hf	3.61	5.52	4.83	4.75	5.19	5.67	5.84	5.54	5.55	6.13	5.2
Th	24.5	19.08	28.79	25.62	16.42	21.08	15.66	15.02	17.06	16.6	17.02
U	1.73	1.59	2.85	1.39	1.37	1.79	1.59	1.98	1.46	1.79	2.32
ΣREE	163.68	214.65	241.46	211.89	256.83	219.56	265.19	284.74	199.12	269.81	272.11
LREE	152.75	191.77	209.98	180.83	222.05	189.35	234.19	255.53	173.88	244.2	244.02
HREE	10.93	22.89	31.48	31.05	34.78	30.21	31	29.21	25.24	25.62	28.08
LREE/HREE	13.98	8.38	6.67	5.82	6.38	6.27	7.55	8.75	6.89	9.53	8.69
La _N /Yb _N	17.84	10.06	6.77	4.6	6.87	6.2	7.73	10.87	7.69	11.92	10.6
δEu	0.54	0.44	0.21	0.21	0.42	0.37	0.6	0.55	0.49	0.61	0.55
δCe	1.03	0.88	1	1.12	0.92	0.87	0.94	0.88	0.92	0.99	0.93
Mg [#]	9.37	11.93	4	5.01	7.27	8.89	8.28	8.44	6.07	7.14	4.53
σ	1.99	1.8	1.95	1.67	1.73	1.92	1.71	1.77	1.84	1.66	2.22
Q	36.85	36.26	38.97	40.1	34.72	34	31.8	34.56	36.56	34.9	34.1
An	2.33	4.33	1.7	2.09	7.64	6.93	9.9	4.07	1.46	4.93	3.09
Ab	23.7	26.68	22.6	29.13	28.83	28.41	30.22	32.81	35.53	34.9	28.43

Table 1 (continued)

Sample	BN5208-1	BPM666-2-7-2	BPM888-2-1	BPM888-3-1	BPM888-5-1	BPM888-11-1	BPM911-4-1	BPM911-5-1	BN4405-DY	BPM911-6-1	BPM911-12-1
Component	1	2	3	4	5	6	7	8	9	10	11
C	1.8	1.81	1.61	1.57	0.47	0.35	0	1.81	1.02	1.72	1.22
Hy	3.15	3.47	1.56	1.47	2.93	2.46	0	3.34	2.34	2.9	0.92
Ilm	0.27	0.36	0.19	0.17	0.34	0.34	0.46	0.45	0.26	0.45	0.36
Mt	0.61	0.49	1.12	0.76	1.44	1.13	2.64	1.91	0.84	1.87	2.13
Ap	0.06	0.1	0.03	0.03	0.09	0.08	0.13	0.14	0.04	0.14	0.09
Zr	0.02	0.04	0.03	0.03	0.03	0.04	0.04	0.04	0.04	0.04	0.03
DI	91.78	89.43	93.78	93.89	87.08	88.7	82.82	88.28	94.05	87.97	92.18
A/CNK	1.16	1.15	1.15	1.14	1.03	1.02	0.88	1.15	1.09	1.14	1.1

Sample	NCH-HSY3-1	NCH-HSY6	NCH-HSY7	NCH-HSY4	NCH-HSY5
Component	12	13	14	15	16
SiO ₂	53.93	55.84	55.27	54.25	54.33
TiO ₂	1.16	1.13	1.14	1.16	1.19
Al ₂ O ₃	16.46	17.12	16.79	16.5	16.43
Fe ₂ O ₃	2.59	2.75	2.98	2.36	2.27
FeO	5.75	5.2	5.25	5.85	5.9
MnO	0.13	0.13	0.13	0.13	0.14
MgO	4.9	3.76	4	4.73	4.66
CaO	7.8	6.49	6.34	7.99	7.86
Na ₂ O	2.68	3.23	3.19	2.68	2.7
K ₂ O	1.39	1.46	1.63	1.33	1.5
P ₂ O ₅	0.31	0.3	0.3	0.31	0.31
LOI	2	1.75	2.12	1.79	1.76
Total	99.1	99.16	99.14	99.08	99.05
Rb	33.14	38.65	45.23	32.62	34.81
Sr	702.34	685.01	685.22	695.60	713.78
Y	20.13	20.78	18.21	18.87	18.79
Zr	128.67	138.18	133.67	129.75	130.83
Nb	6.84	8.68	7.90	7.38	7.96
Ba	269.06	319.05	374.12	270.08	338.59
La	26.11	29.18	25.00	24.48	24.69
Ce	53.57	58.34	50.06	50.72	51.03
Pr	7.76	8.10	7.03	7.44	7.36
Nd	30.01	30.61	26.51	28.69	28.73
Sm	6.03	6.01	5.16	5.72	5.69
Eu	1.69	1.63	1.49	1.58	1.56
Gd	5.39	5.48	4.68	5.17	4.98
Tb	0.84	0.85	0.72	0.78	0.78
Dy	4.28	4.32	3.79	4.04	4.09
Ho	0.81	0.83	0.71	0.76	0.75
Er	2.06	2.19	1.87	1.97	1.95
Tm	0.29	0.31	0.27	0.28	0.28
Yb	1.82	1.94	1.67	1.76	1.69
Lu	0.27	0.29	0.25	0.25	0.26
Hf	3.57	3.74	3.40	3.49	3.40
Th	4.86	6.06	5.54	5.44	5.22
U	0.50	0.56	0.69	0.48	0.49

Table 1 (continued)

Sample	NCH-HSY3-1	NCH-HSY6	NCH-HSY7	NCH-HSY4	NCH-HSY5
Component	12	13	14	15	16
ΣREE	140.92	150.07	129.22	133.65	133.84
LREE	125.17	133.87	115.25	118.63	119.06
HREE	15.76	16.21	13.96	15.01	14.78
LREE/HREE	7.94	8.26	8.26	7.90	8.06
La _N /Yb _N	10.29	10.79	10.74	9.98	10.48
δEu	0.91	0.87	0.93	0.89	0.90
δCe	0.92	0.93	0.93	0.92	0.93
Mg#	0.52	0.47	0.47	0.51	0.51
σ	1.4	1.62	1.77	1.33	1.45
Q	8.76	10.92	9.93	9.12	8.78
An	29.64	28.65	27.5	29.87	29.07
Ab	23.35	28.06	27.83	23.31	23.48
Hy	16.31	14.67	15.34	15.94	15.84
Mt	3.87	3.97	4.15	3.52	3.38
Ap	0.74	0.71	0.72	0.74	0.74
DI	40.58	47.84	47.69	40.51	41.37
A/CNK	0.85	0.95	0.94	0.84	0.84

Note. 1–6, Rongguo Longba granite; 7–11, Garongcuo granite porphyry; 12–16, Nuocang area basaltic andesitic crystal tuff (data from (Jiang, 2018)); Q, quartz; An, anorthite; Ab, albite; Or, orthoclase; C, corundum; Hy, hypersthene; Ilm, ilmenite; Mt, magnetite; Ap, apatite; Zr, zircon; Chr, chromite. Mg[#] = 100 × Mg²⁺/(Mg²⁺ + Fe²⁺), in which Mg²⁺, Fe²⁺ are molar fractions; (2) A/CNK = molar Al₂O₃/(CaO + Na₂O + K₂O); (3) σ = (Na₂O + K₂O)²/(SiO₂ – 43)(wt.-%); (4) DI = Qz + Or + Ab + Ne + Lc + Kp.

X-ray fluorescence spectrometer with accuracy better than 1%. Trace- and rare-earth element analysis was performed using an ELEMENT-2 mass spectrometer with accuracy better than 2%. The detailed analysis process can be found in (Fei et al., 2014).

GEOCHEMICAL AND ISOTOPIC COMPOSITION

Table 1 shows the representative major-, trace-, and rare-earth element compositions of rock samples from the Nuocang area of Tibet.

Major and trace elements. Major and trace elements from 11 granitoid samples, taken from two Paleocene intrusions (Rongguo Longba and Garongcuo), as well as five basaltic andesitic crystal tuff samples from the Dianzhong Formation in Nuocang (data from (Jiang, 2018)), are listed in Table 1 (BPM911-6-1 and

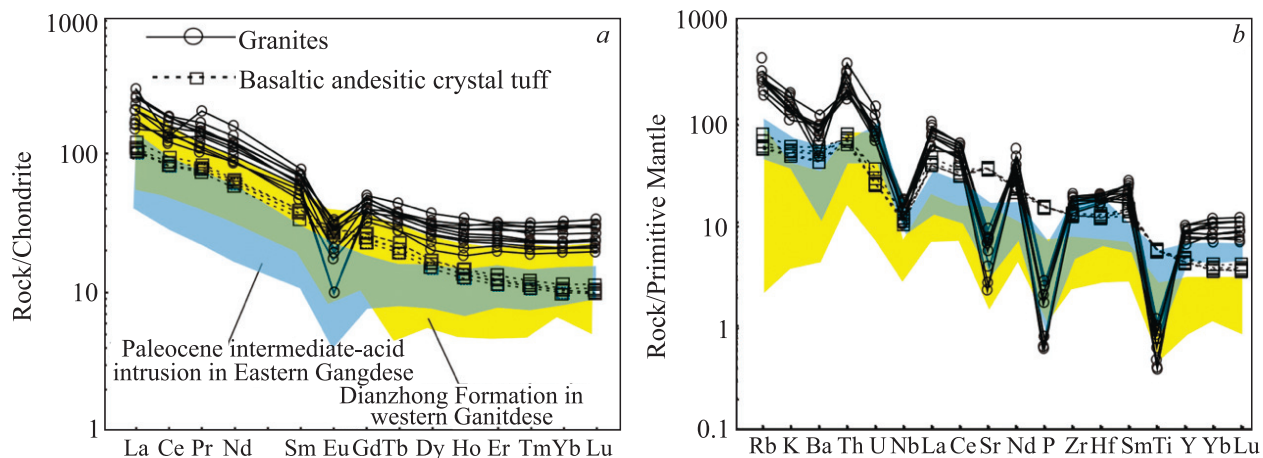


Fig. 5. Chondrite-normalized REE patterns (a, normalization values from (Sun and McDonough, 1989)) and primitive mantle-normalized trace-element patterns (b) for the Nuocang intermediate-acid dikes (normalization values from (Pearce et al., 1984)).

Table 2. The zircon Hf isotopic compositions of the Nuocang area granitic rock, southern Tibet

Spot number	Age, Ma	Lu, ppm	Hf, ppm	$^{176}\text{Yb}/^{177}\text{Hf}$	$^{176}\text{Lu}/^{177}\text{Hf}$	2σ	$^{176}\text{Hf}/^{177}\text{Hf}$	2σ	$\varepsilon_{\text{Hf}}(0)$	$\varepsilon_{\text{Hf}}(t)$	t_{DMI}/Ma	$T_{\text{DM}}^{\text{c}}/\text{Ma}$	$f_{\text{Lu/Hf}}$
BN5208-1-01	62.1	80.6	12,965	0.040752	0.001521	0.000012	0.282569	0.000023	-7.18	-5.95	980	1510	-0.95
BN5208-1-03	62.3	95.2	11,963	0.048136	0.001651	0.000007	0.282621	0.000015	-5.34	-4.12	909	1394	-0.95
BN5208-1-05	61.8	80.5	12,940	0.027172	0.001032	0.000005	0.282542	0.000019	-8.12	-6.88	1005	1570	-0.97
BN5208-1-06	63.1	72	13,021	0.025714	0.000899	0.000001	0.282583	0.000014	-6.67	-5.41	944	1477	-0.97
BN5208-1-07	64.5	84.6	13,098	0.025021	0.000918	0.000015	0.282595	0.000015	-6.25	-5	928	1451	-0.97
BN5208-1-09	61.3	73.8	12,767	0.041254	0.001452	0.000009	0.28258	0.000017	-6.79	-5.52	962	1485	-0.96
BN5208-1-10	63.1	80.6	13,351	0.045725	0.001701	0.000023	0.282529	0.000023	-8.59	-7.38	1042	1601	-0.95
BN5208-1-18	64.5	90.6	11,636	0.038644	0.001425	0.000029	0.282555	0.000019	-7.69	-6.47	998	1543	-0.96
BN5208-1-19	61.7	69.3	15,767	0.04584	0.001592	0.000033	0.28255	0.000015	-7.86	-6.63	1009	1553	-0.95
BN5208-1-20	62.0	71.2	13,672	0.030678	0.001079	0.000024	0.282571	0.000016	-7.11	-5.84	966	1505	-0.97
BN5208-1-22	61.3	85	13,232	0.031842	0.001053	0.000017	0.282594	0.000017	-6.3	-5.04	933	1454	-0.97
BN4405-Dy-01	61.1	95.9	8977	0.000182	0.00156	0.000007	0.282562	0.00002	-7.42	-6.25	991	1529	-0.95
BN4405-Dy-06	67.3	55.5	8778	0.000141	0.001308	0.000003	0.282604	0.000016	-5.94	-4.81	925	1435	-0.96
BN4405-Dy-07	59.9	70.1	9758	0.000157	0.001164	0.000007	0.282641	0.000021	-4.65	-3.61	870	1356	-0.96
BN4405-Dy-08	61.3	65	9739	0.001846	0.002081	0.000058	0.282551	0.000017	-7.8	-6.61	1021	1553	-0.94
BN4405-Dy-10	61.8	79.9	9064	0.000388	0.001197	0.000024	0.282616	0.000015	-5.53	-4.24	906	1404	-0.96
BN4405-Dy-11	62.3	100	9806	0.000286	0.00141	0.000013	0.28252	0.000022	-8.91	-7.48	1047	1615	-0.96
BN4405-Dy-12	61.5	89.7	8399	0.000193	0.001215	0.00001	0.282601	0.000018	-6.05	-4.35	927	1426	-0.96
BN4405-Dy-13	62.4	103.9	7555	0.000203	0.001128	0.000004	0.282587	0.000018	-6.55	-5.37	945	1473	-0.97
BN4405-Dy-15	59.9	119.3	7540	0.000172	0.000936	0.000005	0.282583	0.000017	-6.68	-5.37	945	1476	-0.97
BN4405-Dy-16	61.1	77.3	8844	0.00014	0.001168	0.000006	0.282545	0.000017	-8.03	-6.8	1005	1565	-0.96
BN4405-Dy-17	58.0	61.4	9414	0.000306	0.001409	0.000009	0.282578	0.000021	-6.85	-5.62	964	1490	-0.96

BPM911-12-1 from (Wang et al., 2017)). The major-element characteristics of the two granite rock samples are not significantly different. SiO_2 content ranges from 70.47 to 77.11 wt.%; Al_2O_3 , K_2O , P_2O_5 , TiO_2 , and MgO contents range from 12.34 to 13.41 wt.%, from 3.02 to 5.38 wt.%, from 0.01 to 0.06 wt.%, from 0.09 to 0.24 wt.%, and from 0.06 to 0.24 wt.%, respectively; the $\text{K}_2\text{O}/\text{Na}_2\text{O}$ ratio of the samples varies between 0.89 and 2.0; the Rittmann index ranges from 1.67 to 1.99, indicating a calc-alkaline rock affinity [$\delta = (\text{Na}_2\text{O} +$

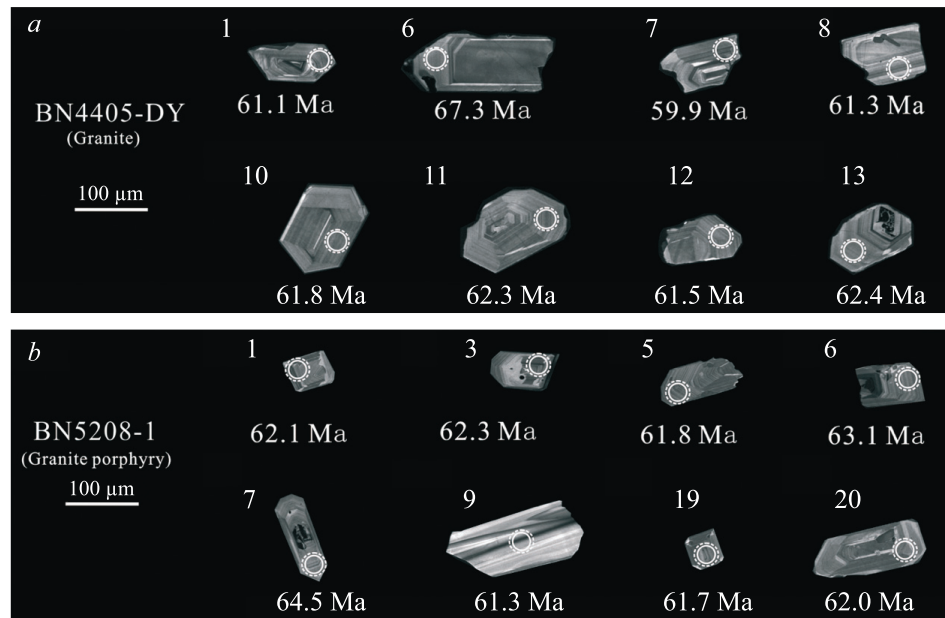


Fig. 6. Cathodoluminescence images of selected granite zircons (BN5208-1) (a) and granite porphyry zircons (BN4405-Dy) (b). Solid and dashed circles show the locations for U-Pb dating and Hf isotope dating, respectively.

Table 3. LA ICP MS zircon U-Pb dating analytical data on granite samples

Spot	Pb ($\times 10^{-6}$)	Th	U	Th/U	$^{207}\text{Pb}/^{206}\text{Pb}$	$^{207}\text{Pb}/^{235}\text{U}$	$^{207}\text{Pb}/^{238}\text{U}$	Ratio	$\pm 1\sigma$	Ratio	$\pm 1\sigma$	Ratio	$\pm 1\sigma$	Age, Ma	$\pm 1\sigma$	Age, Ma	$\pm 1\sigma$
BN4405-DY Granite porphyry, 85°09'10"E, 30°24'03"N																	
-1	2.29	146.62	206.61	0.71	0.0524	0.0061	0.0639	0.0070	0.0095	0.00361	0.002730	0.000185	62.9	6.7	61.1	2.3	55.1
-2	3.14	226.01	241.48	0.94	0.0497	0.0050	0.0714	0.0071	0.0105	0.000310	0.002991	0.000187	70.1	6.7	67.3	2.0	60.4
-6	1.54	101.51	143.83	0.71	0.0485	0.0078	0.0593	0.0074	0.0093	0.000534	0.002632	0.000294	58.5	7.1	59.9	3.4	53.1
-7	2.83	192.21	262.91	0.73	0.0451	0.0055	0.0596	0.0074	0.0095	0.000359	0.002389	0.000211	58.8	7.1	61.3	2.3	48.2
-8	2.58	159.75	236.15	0.68	0.0470	0.0047	0.0616	0.0062	0.0096	0.000313	0.002876	0.000179	60.7	6.0	61.8	2.0	58.1
-10	2.38	148.86	211.05	0.71	0.0481	0.0051	0.0626	0.0063	0.0097	0.000251	0.003035	0.000215	61.7	6.0	62.3	1.6	61.3
-11	3.21	228.58	276.53	0.83	0.0506	0.0057	0.0657	0.0065	0.0096	0.000333	0.003389	0.000269	64.6	6.2	61.5	2.1	68.4
-12	2.17	124.15	184.85	0.67	0.0484	0.0039	0.0689	0.0062	0.0097	0.000510	0.003991	0.000431	67.6	5.9	62.4	3.3	80.5
-13	1.71	129.81	158.90	0.82	0.0457	0.0068	0.0574	0.0094	0.0093	0.000509	0.002723	0.000388	56.7	9.0	59.9	3.3	55.0
-15	2.59	181.23	223.64	0.81	0.0526	0.0074	0.0679	0.0090	0.0095	0.000355	0.003057	0.000203	66.7	8.5	61.1	2.3	61.7
-16	1.98	116.91	188.46	0.62	0.0496	0.0056	0.0598	0.0055	0.0090	0.000399	0.002863	0.000244	59.0	5.3	58.0	2.5	57.8
-17	2.78	173.14	248.93	0.70	0.0504	0.0080	0.0661	0.0113	0.0095	0.000433	0.002892	0.000217	65.0	10.8	60.9	2.8	58.4
-18	5.47	154.47	179.82	0.86	0.0527	0.0057	0.0696	0.0067	0.0098	0.000299	0.002855	0.000320	68.3	6.3	63.1	1.9	57.6
-19	3.64	112.37	139.48	0.81	0.0481	0.0065	0.0618	0.0079	0.0096	0.000358	0.002874	0.000425	60.9	7.5	61.3	2.3	58.0
-20	3.48	101.85	134.86	0.76	0.0440	0.0057	0.0623	0.0084	0.0100	0.000348	0.00297	0.000325	61.3	8.0	63.8	2.2	59.1
-22	5.95	182.10	169.59	1.07	0.0475	0.0076	0.0603	0.0082	0.0097	0.000380	0.002662	0.000255	59.4	7.8	62.1	2.4	53.7
-24	3.60	108.86	163.25	0.67	0.0655	0.0075	0.0860	0.0112	0.0095	0.000335	0.002787	0.000359	83.8	10.4	61.2	2.1	56.3
-25	7.19	228.15	228.65	1.00	0.0413	0.0036	0.0547	0.0052	0.0095	0.000199	0.002437	0.000222	54.1	5.0	61.2	1.3	49.2
-26	3.27	106.67	135.01	0.79	0.0531	0.0071	0.0695	0.0091	0.0097	0.000338	0.002551	0.000303	68.2	8.7	62.3	2.2	51.5
-29	4.68	192.33	192.82	1.00	0.0425	0.0049	0.0560	0.0062	0.0098	0.000316	0.002753	0.000329	55.3	6.0	63.0	2.0	55.6
-31	7.59	265.64	241.34	1.10	0.0632	0.0081	0.0811	0.0099	0.0096	0.000308	0.003019	0.000339	79.1	9.3	61.5	2.0	60.9
-32	5.49	174.37	134.20	1.30	0.0480	0.0052	0.0638	0.0064	0.0098	0.000291	0.003491	0.000353	62.8	6.1	62.9	1.9	70.4
-33	7.80	280.18	225.00	1.25	0.0593	0.0066	0.0754	0.0080	0.0094	0.000334	0.002963	0.000233	73.8	7.6	60.2	2.1	59.8
-34	12.44	342.75	301.10	1.14	0.0481	0.0047	0.0638	0.0063	0.0097	0.000277	0.003302	0.000281	62.8	6.0	62.2	1.8	66.6
-35	4.65	139.54	145.58	0.96	0.0483	0.0050	0.0616	0.0064	0.0094	0.000255	0.003053	0.000348	60.7	6.1	60.1	1.6	61.6
-36	3.87	122.63	147.96	0.83	0.0544	0.0074	0.0684	0.0085	0.0096	0.000334	0.002782	0.000336	67.1	8.1	61.4	2.1	56.1
-37	3.14	98.17	90.77	1.08	0.0406	0.0081	0.0544	0.0098	0.0100	0.000469	0.002702	0.000308	53.8	9.5	63.8	3.0	54.5
BN5208-1 granite 85°00'00"E, 30°27'57"N																	
-1	5.62	188.70	239.64	0.79	0.0483	0.0037	0.0645	0.0050	0.0097	0.000203	0.002674	0.000210	63.4	4.8	62.2	1.3	54.0
-3	5.06	195.34	241.72	0.81	0.0538	0.0057	0.0675	0.0060	0.0094	0.000183	0.002220	0.000172	66.3	5.8	60.1	1.2	44.8

-5	231.75	278.59	0.83	0.0543	0.0051	0.0068	0.0093	0.000262	0.0002355	0.000241	69.3	4.9
-6	5.86	211.22	258.73	0.82	0.0566	0.0086	0.0745	0.0117	0.0096	0.000286	0.0002400	60.5
-7	4.75	183.47	217.38	0.84	0.0474	0.0047	0.0623	0.0065	0.0095	0.000418	0.002241	7.2
-8	4.92	184.69	229.50	0.80	0.0490	0.0053	0.0621	0.0058	0.0094	0.000216	0.002351	4.5
-9	6.38	212.07	264.27	0.80	0.0508	0.0039	0.0685	0.0051	0.0098	0.000253	0.002719	4.1
-11	5.01	246.16	336.57	0.73	0.0560	0.0033	0.0739	0.0044	0.0097	0.000214	0.002930	2.9
-13	5.84	255.07	388.45	0.66	0.0563	0.0036	0.0735	0.0044	0.0097	0.000187	0.003367	3.1
-15	3.80	184.34	283.21	0.65	0.0609	0.0046	0.0758	0.0051	0.0096	0.000251	0.003191	3.3
-16	4.59	212.73	326.45	0.65	0.0577	0.0038	0.0775	0.0047	0.0098	0.000216	0.003294	3.4
-17	4.86	196.76	333.04	0.59	0.0565	0.0053	0.0759	0.0067	0.0101	0.000271	0.003415	4.6
-18	4.96	244.76	294.28	0.83	0.0590	0.0045	0.0782	0.0058	0.0101	0.000281	0.003649	3.4
19	4.23	196.54	295.12	0.67	0.0556	0.0047	0.0715	0.0060	0.0096	0.000226	0.003424	4.6
-20	3.82	175.49	266.89	0.66	0.0578	0.0052	0.0758	0.0069	0.0098	0.000308	0.003321	4.1
-21	7.54	443.54	397.17	1.12	0.0572	0.0051	0.0761	0.0063	0.0100	0.000282	0.003616	3.3
-22	4.50	226.43	322.73	0.70	0.0587	0.0049	0.0725	0.0048	0.0096	0.000259	0.003150	3.6
-23	4.65	202.77	310.82	0.65	0.0577	0.0042	0.0775	0.0059	0.0099	0.000265	0.003418	5.9
-24	6.05	220.12	484.42	0.45	0.0539	0.0034	0.0711	0.0040	0.0101	0.000236	0.003146	3.3
-25	3.66	94.51	336.00	0.28	0.0566	0.0041	0.0720	0.0046	0.0096	0.000253	0.003222	5.2
-26	3.57	158.55	272.30	0.58	0.0516	0.0047	0.0658	0.0055	0.0097	0.000226	0.003358	4.5
-27	3.39	171.63	267.28	0.64	0.0588	0.0059	0.0699	0.0060	0.0096	0.000328	0.003000	4.0

$K_2O)^2/(SiO_2 - 43)$]. The DI Index ranges from 82.82 to 94.05, indicating that the rock is highly fractionated. The analyzed samples have a high $Na_2O + K_2O$ content, between 6.91 and 8.23 wt.%. On the SiO_2 vs. $Na_2O + K_2O$ (TAS) diagram (Fig. 6a), all the samples plot in the granite field, and with the A/CNK (molar $Al_2O_3/CaO + K_2O$) ratios varying between 0.88 and 1.16 on the SiO_2-KO_2 diagram, all fall into the high-K calc-alkaline series classification (Fig. 7d). Based on the dating results of this study, there is no clear rule governing changes in the production of the above major elements. The granitoid and eastern Gangdese intrusive rock samples are compositionally analogous to the volcanic rocks of the Dianzhong Formation in the Nuocang area (Fig. 4a).

The Dianzhong Formation basaltic andesitic crystal tuff is characterized by low SiO_2 and K_2O contents ranging from 53.93 to 55.84 wt.% and from 1.33 to 1.63 wt.%, respectively, as well as a low A/CNK ratio of 0.85–0.95, high Na_2O , MgO , TiO_2 , and FeO^T contents ranging from 2.68 to 3.3 wt.%, from 3.76 to 4.9 wt.%, from 1.13 to 1.19 wt.%, and from 6.1 to 8.1 wt.%, respectively. On the SiO_2 vs. $Na_2O + K_2O$ (TAS) diagram (Fig. 4c), all the samples plot onto the basalt–andesite field. The $Mg^{\#}$ value ranges from 47 to 52, indicating the basic volcanics.

The Rongguo Longba granite and the Garongguo granite porphyry generally have similar REE patterns displaying LREE enrichment and obvious fractionated HREE relative to LREE–HREE = 5.82–13.98, $La_N/Yb_N = 4.6$ –17.84, $\delta Eu = 0.21$ –0.61, with a negative Eu anomaly (Fig. 5a). On the primitive mantle-normalized spider diagram (Fig. 5b), all the granite and granite porphyry samples are characterized by enrichments in incompatible elements and LILE, such as Rb, Ba, Th, and K, and pronounced depletions in HFSE, such as Nb, Sr, Ti, and P. In terms of trace-element composition, the samples in this study are similar to igneous rocks of the eastern Gangdese Belt in Tibet. The basic volcanic rocks rare-earth partition curve is smooth. The samples exhibit weak negative Eu anomalies ($Eu/Eu^* = 0.87$ –0.91) and fractionated REE patterns characterized by $(La/Yb)_N$ ratios of 9.98–10.79 (Table 1). As shown on the primitive mantle-normalized spider diagram, these samples are characterized by enrichments in incompatible elements and LILE, such as

Rb and K, and depletion in HFSE, such as Nb and U (Fig. 5b). Sr and Y contents are high, ranging from 685 to 713.8 ppm and from 18.8 to 20.8 ppm, respectively.

Lu–Hf isotopic characteristics. The research team conducted Lu–Hf isotope analysis with zircon age of the granite porphyry (BN4405-DY) and granite (BN5208-1). The results are given in Table 2, and the positions are shown in Fig. 6. The zircon $^{176}\text{Hf}/^{177}\text{Hf}$ ratio of the granite porphyry (BN4405-DY) is 0.282520–0.282641; the $\epsilon_{\text{Hf}}(t)$ value is –7.38–4.12; the mantle model age is 870–1047 Ma, and the crustal model age (T_{DM}^{C}) is 1356–1615 Ma. The zircon $^{176}\text{Hf}/^{177}\text{Hf}$ ratio of granite (BN5208-1) is 0.282529–0.282621; the $\epsilon_{\text{Hf}}(t)$ value is 7.48–3.61; the mantle model age is 928–1042 Ma, and the crustal model age is 1394–1601 Ma.

Isotope geochronology

One Nuocang granite sample (BN5208-1) and one granite porphyry sample (BN4405-DY) were selected for zircon U–Pb age analysis. Most of the zircons in the samples were transparent and subhedral, with lengths of 50–150 μm . Some grains exhibited concentric zoning, and some grains demonstrated a core–mantle structure (Fig. 6). The granite Th and U contents (BN5208-1) were 94.51×10^{-6} – 443.54×10^{-6} and 266.89×10^{-6} – 484.42×10^{-6} , respectively, and the Th/U ratios were 0.28–1.12. The granite porphyry Th and U contents (BN4405-DY) were 98.17×10^{-6} – 342.75×10^{-6} and 90.77×10^{-6} – 262.91×10^{-6} , respectively, while its Th/U ratios were 0.63–1.3. The Th/U ratios were all greater than 0.1 (Table 3), and there was positive correlation between Th and U contents. These characteristics indicate that the zircons evaluated in this study are magmatic (Hoskin and Schaltegger, 2003; Wu and Zheng, 2004). The weighted mean zircon U–Pb ages for the granite (BN5208-1) and granite porphyry samples (BN4405-DY) are 61.86 ± 0.8 Ma (MSWD = 0.60) and 62.17 ± 0.67 Ma (MSWD = 0.052), respectively (Fig. 7).

DISCUSSION

Age of rock formation

The Nuocang area granite porphyry (BN4405-DY) and granite samples (BN5208-1) have weighted mean ages of 61.86 ± 0.8 and 62.17 ± 0.67 Ma, respectively, suggesting that the latest emplacement starting date for Paleocene granitoids was at 61.86 ± 0.8 Ma, in the Paleocene. The basaltic andesitic crystal tuff interlayer of the Dianzhong Formation is also present in the Nuocang area. According to the previous research, the Dianzhong Formation formed in the western Gangdese Belt at 51.6–64.8 Ma in the Dajiacuo area (Geological Survey of Jiangxi Province, 2015), at 61–63.9 Ma in the Coqen area (Hu et al., 2007), at 58.55–60.07 Ma in the Coqen–Angren area (Wen et al., 2008) and, by its olivine tholeiite formation, at 58.4–60.1 Ma in the Shiquanhe area. To sum up, the basaltic andesitic crystal tuff is likely to have formed at 60 Ma, which corresponds to the formation age of granites in the study area. The previous studies showed that the India–Eurasia collision was simultaneously in the eastern and western directions, with the initial collision at 65 Ma (Hou et al., 2008; Mo et al., 2007a,b; Dong et al., 2011). The Linzizong Formation volcanic rocks represent the tectonic environment of the initial collision, and its age likewise corresponds to that of the granitoids in this study. Meanwhile, evi-

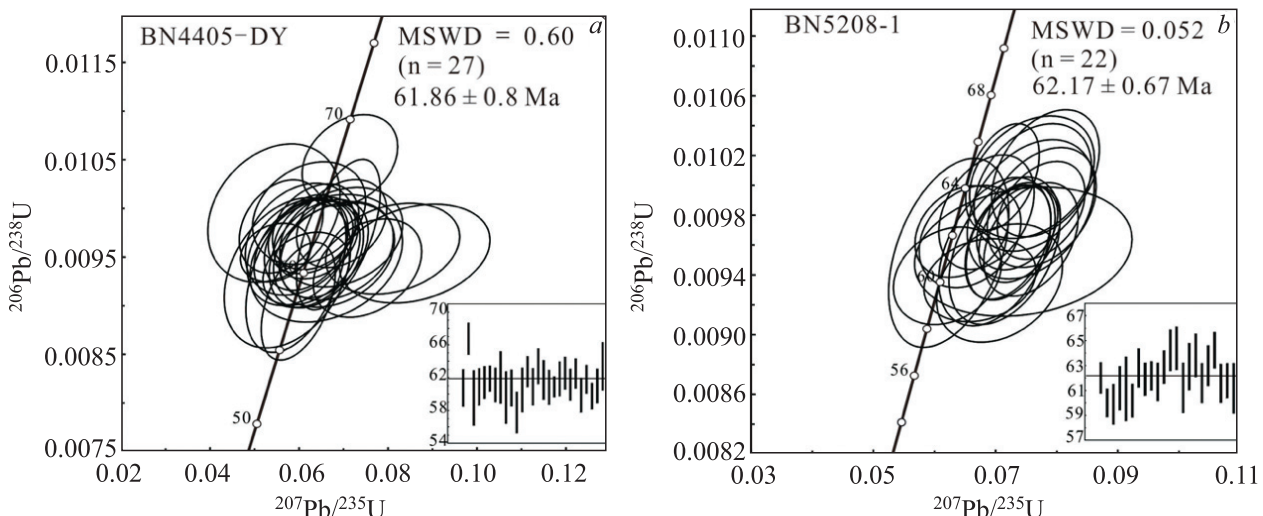


Fig. 7. ICP MS zircon U–Pb dating concordia diagrams for granite samples (BN4405-DY and BN5208-1) from the Nuocang area, Tibet.

Table 4.

The Paleocene Gangdese igneous rocks: locations and ages

Structurallocation	Number	Sample	Locality	Longitude(°E)	Latitude(°N)	Rock type	Age, Ma	Ref.
Eastern Gangdese	1	LZ1104	Linzhou basin	91°01.9'–91°11.9'	29°54.9'–29°58.2'	granite porphyry	55.1	Dong et al., 2015
	2	LZ1106	Linzhou basin	91°01.9'–91°11.9'	29°54.9'–29°58.2'	granite porphyry	57.8	Dong et al., 2015
	3	LZ1110	Linzhou basin	91°01.9'–91°11.9'	29°54.9'–29°58.2'	granite porphyry	61.1	Dong et al., 2015
	4	LZ1113	Linzhou basin	91°01.9'–91°11.9'	29°54.9'–29°58.2'	granite porphyry	59.8	Dong et al., 2015
	5	LZ1108	Linzhou basin	91°01.9'–91°11.9'	29°54.9'–29°58.2'	Bi-granodiorite porphyrite	62.4	Dong et al., 2015
	6	NML03-1	Nannulin			Diorite	62.4	Zhu et al., 2011
	7	2003T363	Linzhou basin			trachybasalt	52.54	Yue et al., 2006
	8	2003T363	Linzhou basin			trachybasalt	52.9	Yue et al., 2006
	9	BLZ-02	Linzhou basin			granite porphyry	60.3	Wang et al., 2006
	10	T0889-D	Riduo			granodiorite porphyrite	62.7	Wang et al., 2019
	11	T0889-G	Riduo			granite	59.5	Wang et al., 2019
	12	G07a	Zhula	93°18'00"–93°53'40"	30°01'22"–30°11'08"	Bi-monzongranite	63.9	Li et al., 2012
	13	G01	Zhula	93°18'00"–93°53'40"	30°01'22"–30°11'08"	Bi-monzongranite	64.6	Li et al., 2012
	14	G03a	Zhula	93°18'00"–93°53'40"	30°01'22"–30°11'08"	Bi-monzongranite	64.3	Li et al., 2012
	15	XM-1	around Lhasa	92.20°	29.71°	Bi-Q-diorite	64	Lü et al., 2012
	16	XM-2	around Lhasa	92.10°	29.70°	Bi-Q-diorite	65.9	Lü et al., 2012
	17	XM-3	around Lhasa	92.08°	29.71°	Granite	67.2	Lü et al., 2012
	18	XM-4-2	around Lhasa	92.04°	29.72°	Monzogranite	66.6	Lü et al., 2012
	19	XM-5	around Lhasa	91.98°	29.73°	Bi-monzongranite	67.5	Lü et al., 2012
	20	XM-6	around Lhasa	91.96°	29.74°	Monzogranite	68.7	Lü et al., 2012
	21	XM-7	around Lhasa	91.20°	29.63°	Bi-granodiorite	60.3	Lü et al., 2012
	22	XM-8	around Lhasa	91.20°	29.64°	Bi-granodiorite	58.2	Lü et al., 2012
	23	XM-9	around Lhasa	91.16°	29.72°	Bi-monzongranite	57.6	Lü et al., 2012
	24	XM-16	around Lhasa	92.10°	29.71°	Diorite-vein	60	Lü et al., 2012
	25	XM-17	around Lhasa	92.10°	29.71°	Monzogranite	68.4	Lü et al., 2012
Western Gangdese	26	Shiquanhe	Shiquanhe			olivine tholeiite	60.1	1:250,000 Shiquanhe regional report, 2003
	27	Beina	Beina	86°12'30"~86°14'00"	30°05'30"~30°07'00"	granite porphyry	58.4	Jiang, 2018
	28	BN0207	Beina	86°12'30"~86°14'00"	30°05'30"~30°07'00"	granite porphyry	63.2	Jiang, 2018
	29	BN02	Coqen			andesite	63.3	Hu et al., 2011
	30	P3308H1	Ntoucang	85°09'10"	30°24'03"	granite porphyry	61	This study
	31	BN4405-DY	Nuocang	85°00'00"	30°27'57"	granite porphyry	61.8	This study
	32	BN5208-1					62.17	This study

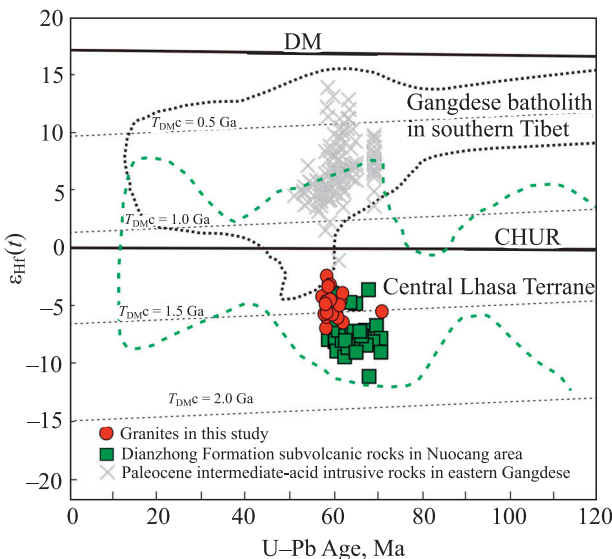


Fig. 8. Gangdese Nuocang granitoid and Paleocene granite $\epsilon_{\text{Hf}}(t)$ values; Gangdese batholith data from (Ji et al., 2012); Nuocang area Dianzhong Formation subvolcanics data from (Jiang, 2018); data on the Paleocene intermediate intrusives of the eastern Gangdese area from (Wang et al., 2006; Lü et al., 2015; Dong et al., 2015).

data on the western Gangdese Belt Dianzhongzu Formation granite porphyry (62 Ma (Jiang, 2018)) and the basic volcanic rocks of the Shiquanhe area (60.1 Ma (Tibet Geological Survey Institute. Shi quan river regional survey report)) indicate simultaneous magmatic activity. It is worth mentioning that the Dianzhong Formation intermediate–acid volcanic rocks and contemporaneous intermediate–acid intrusive rocks of the eastern and western Gangdese Belt exhibit strong geochemical similarities in components, peraluminosity, calc-alkaline classification, trace-element enrichment or depletion, and a right-leaning REE distribution.

Therefore, the Paleocene Nuocang granitoids and basaltic andesitic crystal tuff are Paleocene magmatic events under the influence of the initial continental collision between India and Eurasia.

Tectonic implications

According to zircon U–Pb dating, the granitoids in this study formed in the same basic time interval as the India–Eurasia continental collision, matching the age of collision-related granite porphyry samples from the eastern Gangdese Belt. They also conform to the eastern Gangdese Belt in terms of major and trace elements, major element content, enrichments in LILE (e.g., K, Rb, Ba, Th, and U), and depletions in HFSE (e.g., Nb, P, and Ti) – all these signs of subduction-related igneous activity (Pearce et al., 1984; Condie, 2001; Mo et al., 2003). However, when comparing collision-related granite porphyry with J_{1-2} –K typical subduction arc volcanic rocks (Yeba Formation and Sangri Group) and Miocene (10~18 Ma) adakitic granite porphyry from the

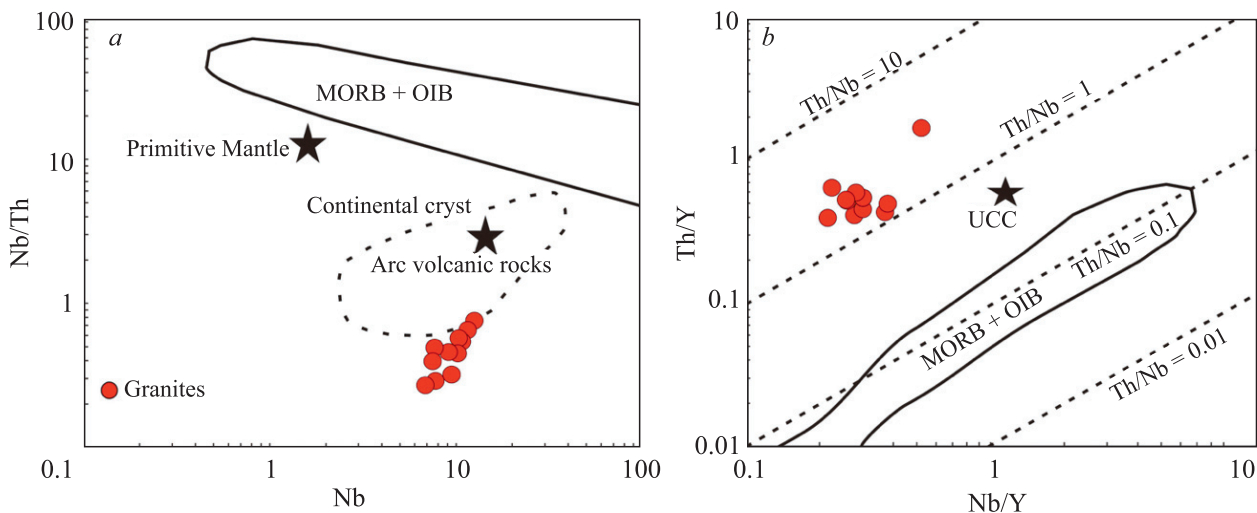


Fig. 9. Nb vs. Nb/Th (a) and Nb/Y vs. Th/Y (b) discrimination diagrams (as in Boztug et al., 2007). Data sources: primitive mantle (Hofmann, 1988); continental crust, MORB, OIB, and arc volcanic rock (Schmidberger and Hegner, 1999).

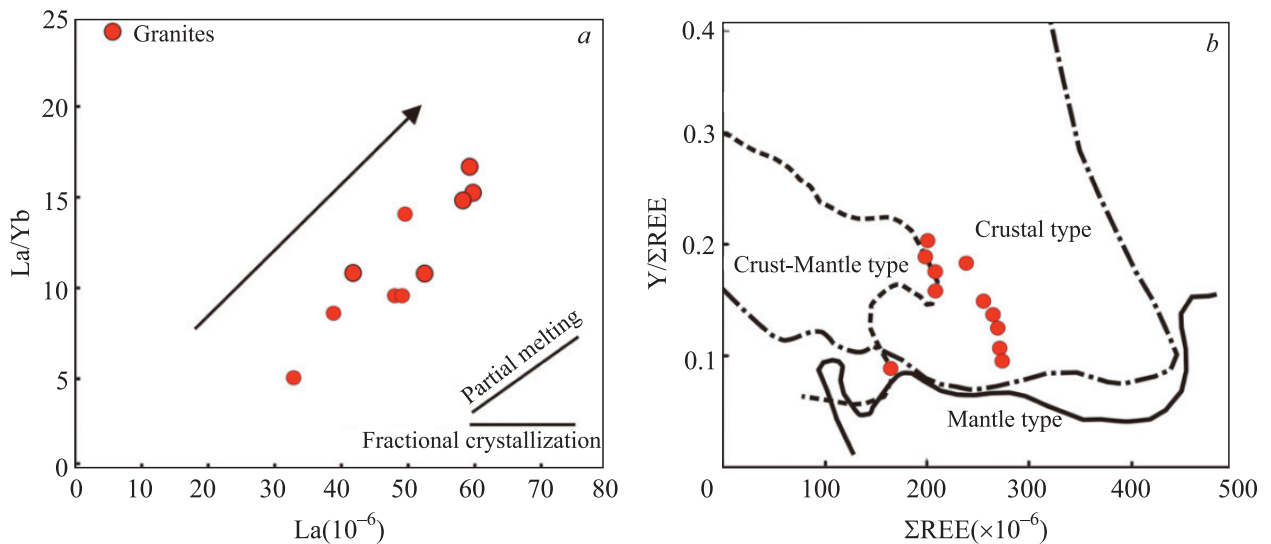


Fig. 10. La vs. La/Yb diagram (a) and Σ REE vs. Y/ Σ REE diagram (b) (as in (Lü et al., 1993)). A, Crust–mantle type granite; B, crust-type granite; C, mantle-type granite.

postcollision crustal extension environment, Wang et al. (2006) found that the Paleocene granite porphyry belonged neither to the adakitic nor to the subduction volcanic rock types. Instead, it should be regarded as intracontinental magmatism transforming from subduction to collision.

The Dianzhong Formation developed a layer of basaltic andesite in the Gangdese Belt. The widespread manifestation of mafic/ultramafic magmatism can be regarded as a collisional thickening environment (Dobretsov et al., 2008, 2010; Dobretsov and Buslov, 2011; Khromykh and Vladimirov, 2013). In addition, an analysis of the volcanic geochemistry of the Dianzhong Formation signifies the extent of crustal material impact on the magma. In particular, the appearance of shoshonite series in the Nianbo and Pana Formations is a strong indicator of intracontinental magmatism (Mo et al., 2003; Dong et al., 2015). The Nuocang granite samples can almost be classified as high-K calc-alkaline, very close to the shoshonite series, implying that the area formed initially in a collision environment.

Petrogenesis

Granite is generally believed to form by the partial melting of crustal materials, while the crustal composition is itself highly heterogeneous. The melting source area may not be pure igneous or pure sedimentary rock. The material heterogeneity of the source area may be inherited by molten magma and even retained in the final crystallized rocks (Wang et al., 2017; Zheng et al., 2019). Zircon Hf isotope analysis is widely used to study the granite rock source properties and characteristics. Positive values of $\epsilon_{\text{Hf}}(t)$ are generally interpreted as juvenile-crust melting or the addition of mantle materials, while granites with negative $\epsilon_{\text{Hf}}(t)$ values are thought to originate from ancient crustal materials (Taylor and McLennan, 1985; Wu et al., 2007). Zircon Hf isotope analysis of the Paleocene Nuocang granite suggests a compositionally uniform source material. The value of $\epsilon_{\text{Hf}}(t)$ ranges from -7.63 to -3.36 , with the T_{DM}^{C} age of 1.4 – 1.6 Ga, indicative of ancient crustal material (Fig. 8). A large variation in $\epsilon_{\text{Hf}}(t)$ values requires an open system to change the ratio of $^{176}\text{Hf}/^{177}\text{Hf}$ in the melt (Kemp et al., 2007). As the zircon Hf isotope ratio does not change with partial melting or fractional crystallization, the heterogeneity of zircon Hf isotopes probably indicates interaction between the more radiogenic Hf mantle provenance and the less radiogenic Hf crustal materials (Bolhar et al., 2008). The granitoids in this study had negative $\epsilon_{\text{Hf}}(t)$ values, in this respect clearly differing from the eastern Gangdese Belt granitoids. This contradicts the previous conclusions that the southern margin of the Gangdese Belt formed from juvenile crust. Some scholars believe this to be the result of ancient crustal melting on the India continent (Dong et al., 2015). However, most believe that the Southern Lhasa Block has an ancient crystalline basement (~ 84 – 88° E) (Hou et al., 2015; Zhang et al., 2017; Jiang, 2018). The postcollision potassic–superpotassic volcanic rocks of the Miocene (8–25 Ma) suggest that it mainly formed by the breaking off of the Neo-Tethys plate during the postcollision stage (Mo et al., 2006, 2009). Then the Indian continental lithosphere subducted to the bottom of the Lhasa Terrane. Therefore, it can be preliminarily concluded that the Indian continental lithosphere did not

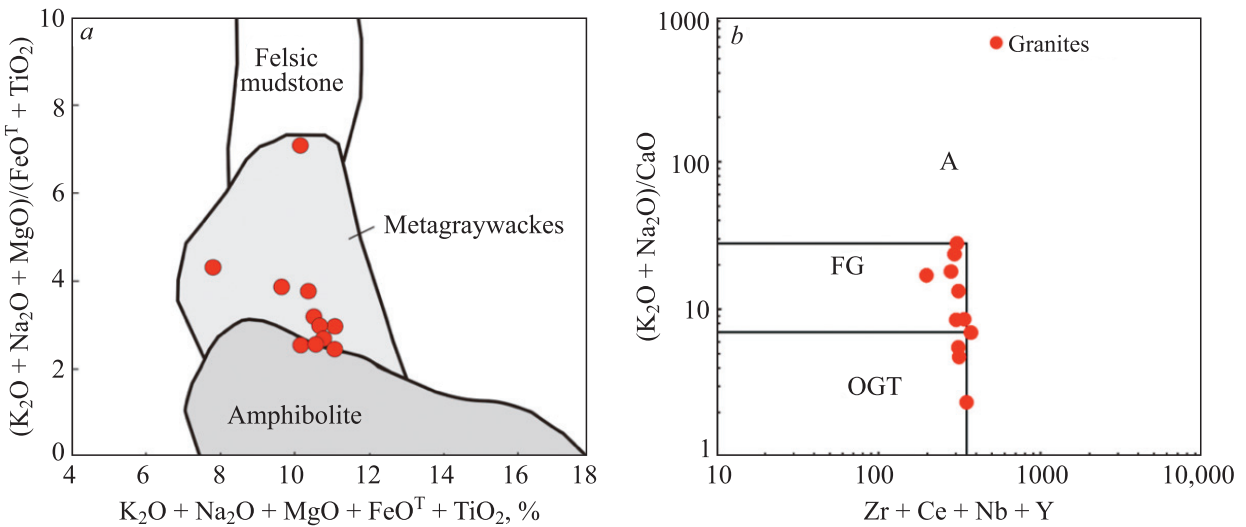


Fig. 11. Geochemical diagrams of $\text{K}_2\text{O} + \text{Na}_2\text{O} + \text{MgO} + \text{FeO}^T + \text{TiO}_2$ vs. $(\text{K}_2\text{O} + \text{Na}_2\text{O})/(\text{MgO} + \text{FeO}^T + \text{TiO}_2)$ and $(\text{K}_2\text{O} + \text{Na}_2\text{O}/\text{CaO}$ vs. $\text{Zr} + \text{Nb} + \text{Ce} + \text{Y}$) (a, Whalen et al. (1987) for the Paleocene granitoids; b, after (Kaygusuz et al., 2008)).

subduct below the Lhasa Terrane at least before 25 Ma. The discrepancy in the $\varepsilon_{\text{Hf}}(t)$ values of the eastern and western Gangdese Belt granitoid samples may be mainly caused by differences in their crystalline basements.

According to the standardized distribution diagram of REE chondrites for the Nuocang granitoids, 11 samples have obvious negative δEu anomalies. Negative δEu anomalies are generally explained in two ways: either by the fractional crystallization of plagioclase in magma or by the existence of a refractory residual phase during partial melting of the crustal source area (Rollinson, 1993; Khromykh et al., 2013). However, the thickness of the Linzizong Group volcanics in the Coqen basin exceeds 2800 m (Ding et al., 2017), and they are widely distributed across the Gangdese Belt. With such a wide distribution, it becomes difficult to explain the formation of the Nuocang granitoids in the relatively short interval proposed by magmatic fractionation. Therefore, the melting of continental crust may have played a more important role during the formation (Dong et al., 2008, 2015; Mo et al., 2009).

In addition, the Nuocang granite porphyry is relatively enriched in LILE (e.g., K, Rb, Ba, Th, and U) and depleted in HFSE (e.g., Nb, P, and Ti) (Fig. 8b). On the one hand, the loss of HFSE may reflect source rock properties, because crustal melts are typically characterized by a loss of HFSE (Xie et al., 2013b); on the other hand, the relatively high loss of Nb, P, and Ti suggests the fractionation and crystallization of Ti-rich minerals—since Ti is not easily combinable and remains in the source area. The P deficit, meanwhile, is caused by apatite separation and crystallization during magmatic evolution and fractionation (Rollinson, 1993; Wu et al., 2003).

On the Nb–Nb/Th diagrams (Fig. 9a), most of the samples are close to continental crust, and far from the primitive mantle and MORB regions, with the same geochemical properties as volcanic-arc rocks. On the Nb/Y–Th/Y diagrams (Fig. 9b), most of the samples fall far from the upper crust but rather between $\text{Th}/\text{Nb} = 1$ and $\text{Th}/\text{Nb} = 10$ trend lines, close to the average composition of the lower and midcrust. In addition, the La/Nb ratios of the samples ranged from 3.8 to 10.7, with an average value of 5.8, far greater than 1.0 and thus differing from mantle-derived magma (De Paolo and Daley, 2000). The low MgO content of the samples (Table 3) likewise implies that the granitoids in the area are derived from the partial melting of crustal materials.

From the La–La/Yb diagram (Fig. 10a), we see that the slope of the distribution curve of the Paleocene granites in the Nuocang area lies closer to the partial melting line. Partial melting may be the main controlling factor in magma genesis.

The granites in this study are thus believed to be formed primarily by the partial melting of crustal materials, where the crustal composition is heterogeneous. That is, the melting source may not be pure igneous or pure sedimentary rock. This material heterogeneity of the source may have been inherited into the magma and retained in the resulting crystallized rocks (Wang et al., 2017; Zheng et al., 2019; Chayka et al., 2020). On the $\Sigma\text{REE} - \text{Y}/\Sigma\text{REE}$ diagram, all the samples fall into the crustal source area (Fig. 10b), indicating the main derivation from partial melting of the lower crust. Comparison between the geochemical compositions of these granitoids and the experimental melt shows an even source material composition. The source rocks may include

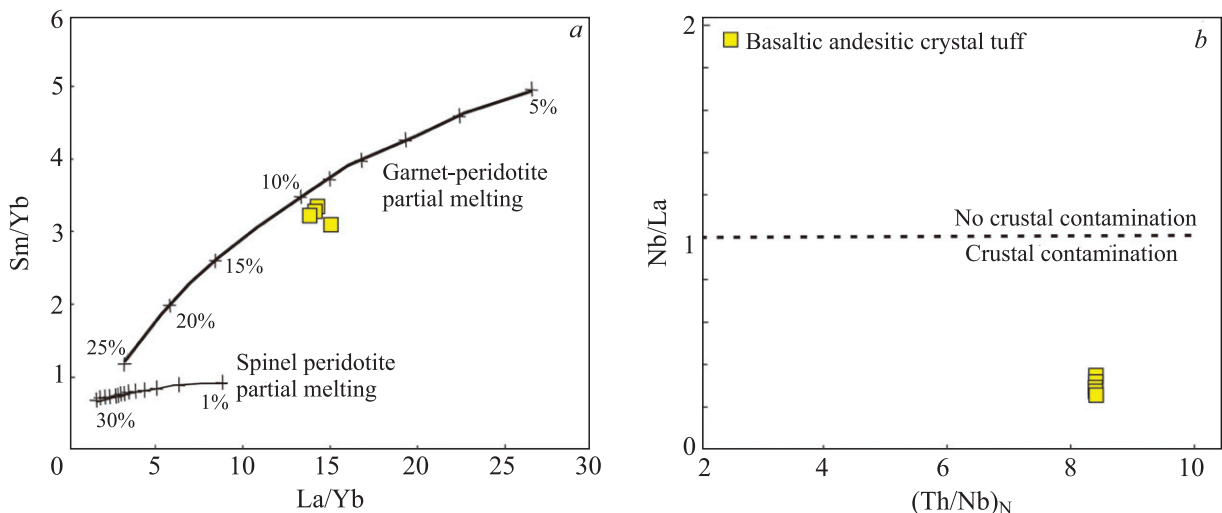


Fig. 12. Plot of La/Yb vs. Sm/Yb (*a*, after (Johnson et al., 1990)) and plot of (Th/Nb)_N vs. Nb/La (*b*, after (Kieffer et al., 2004)); normalized values from (Sun and McDonough, 1989), for the Nuocang area basaltic andesitic crystal tuff samples.

only the ancient crust, dominated by metagraywackes (Fig. 11*a*), which is consistent with the zircon Hf isotope analysis results, which also suggest an even source material composition.

It is generally recognized that the magma originated from melting of the lower crust materials Mg[#] < 40 (Atherton and Petford, 1993) and the partial melting of basalt Mg[#] > 45 (Rapp, 1997). More basic materials than basalt mixed with Mg[#] > 50 (Wu et al., 2003) and direct partial melting of mantle peridotite Mg[#] > 60 (McCarren and Smellie, 1998). The Mg[#] value of the basic rock samples ranges from 47 to 52, with a mean of 50, indicating that the source is not completely crustal, but may have mantle-derived materials mixed in. The La/Yb vs. Sm/Yb diagram shows that possibly 10% of garnet–peridotite in the basaltic andesitic crystal tuff was partially molten (Fig. 12*a*) and contaminated by crust during upward emplacement (Fig. 12*b*).

Dynamic evolution

Prior to the India–Eurasia continental collision, the Neo-Tethys oceanic lithosphere subducted beneath the Eurasian continent at a normal angle to form typical epicontinental arc volcanic rocks (~120–65 Ma). Then, the initial plate collision occurred at 65 Ma. Under the influence of gravity, the Neo-Tethys oceanic lithosphere subducted deeply and rotated in the process. Near the Moho surface, partial melting of the hydrated mantle wedge generated magma upwelling. The intense heat melted the ancient Lhasa crust along with a portion of the mantle-derived magma, producing a wide area of highly differentiated acidic volcanic rock formation – that is, the Linzizong Formation. As the Neo-Tethys lithosphere continued subducting, the Indian Plate pushed below the Eurasia Plate. The uplifting of the subduction zone resulted in an environment of crustal extension and thinning. Crustal decompression, mantle thermal upwelling, and partial melting together produced the basic volcanic interlayer of the Dianzhong Formation.

CONCLUSIONS

(1) The Nuocang granite and granite porphyry yield ages of 61.86 ± 0.8 Ma (MSWD = 0.6) and 62.17 ± 0.67 Ma (MSWD = 0.052), respectively, indicating that these intrusions formed in the early Paleocene. This concurs with the ages of the east Gangdese Belt granitoids, indicating that early Paleocene magmatic activity in the Gangdese Belt was synchronous from east to west;

(2) The Nuocang granites are calc-alkaline to high-K calc-alkaline and metaluminous to peraluminous with a high DI index and a right-leaning REE pattern. They feature enrichments in incompatible elements and LILE – such as Rb, Ba, Th, and K – along with pronounced depletions in HFSE – such as Nb, Sr, Ti, and P;

(3) The granitoid source is derived from the melting of the metagraywackes of the ancient crystalline basement; its basaltic andesitic crystal tuff is derived from garnet–peridotite partial melting and crustal contamination which occurred during the intrusion of upwelling magma.

We thank N.L. Dobretsov and A.E. Izokh for useful discussion.

Projects of 1:50,000 regional geological survey of the Luocang area were mainly undertaken at the Chengdu University of Technology. The Level 2 project uses the Gangdese metallogenic belt base survey items (project code: 1212011221067) and is supported by central funding. Our sincere thanks extend to the members of the Luocang project for their help in the field and their constructive comments and suggestions.

REFERENCES

- Atherton, M.P., Petford, N.**, 1993. Generation of sodium-rich magmas from newly underplated basaltic crust. *Nature* 362 (6416), 144–146.
- Bao, C.H., Ding, F., Wang, Q., Liu, S.H., Xu, F., He, C.X.**, 2014. Lithochemical, geochemical, characteristics and tectonic setting of the volcanic rocks in the Eocene Pana Formation, Linzizong Group, in the Xiongma area, Coqen County, Xizang (Tibet). *Geol. Rev.* 60 (2), 275–284.
- Bolhar, R., Weaver, S.D., Whitehouse, M.J., Palin, J.M., Woodhead, J.D., Cole, J.W.**, 2008. Sources and evolution of arc magmas inferred from coupled O and Hf isotope systematics of plutonic zircons from the Cretaceous Separation Point Suite (New Zealand). *Earth Planet. Sci. Lett.* 268 (3–4), 312–324.
- Boztuğ D., Harlavan, Y., Arehart, G.B., Satır, M., Avcı, N.**, 2007. K-Ar age, whole-rock and isotope geochemistry of A-type granitoids in the Divrii-Sivas region, eastern-central Anatolia, Turkey. *Lithos*, 97(1–2), 193–218.
- Chayka, V.F., Zhitova, L.M., Antsiferova, T.N., Abersteiner, A., Shevko, A.Ya., Izokh, A.E., Tolstykh, N.D., Gora, M.P., Chubarov, V.M., Kamenetsky, V.S.**, 2020. In-situ crystallization and continuous modification of chromian spinel in the “sulfide-poor platinum-group metal ores” of the Norilsk-1 intrusion (Northern Siberia, Russia). *Minerals* 10 (6), 498.
- Chung, S.L., Liu, D.Y., Ji, J.Q., Chu, M.F., Lee, H.Y., Wen, D.J., Lo, C.H., Lee, T.Y., Qian, Q., Zhang, Q.**, 2003. Adakites from continental collision zones: Melting of thickened lower crust beneath southern Tibet. *Geology* 31 (11), 1021–1024.
- Condie, K.C.**, 2001. Mantle Plumes and Their Record in Earth History. Cambridge Univ. Press, London.
- Dewey, J F., Cande, S., Pitman W.C.** 1989. Tectonic evolution of the India/Eurasia collision zone. *Eclat-gae Geol. Helv.* 82 (3), 717–734.
- Ding Feng, Xu Zhongbiao, Liu Shouhang, Li Yue, Gao Jianguo, Fan Yuhang, Li Qing**, 2017. LA-ICP-MS zircon U-Pb ages, petrochemical characteristics and petrogenesis of the volcanic rocks from the Palaeocene—Eocene Nianbo Formation in Chima Area, Coqen County, Xizang (Tibet). *Geol. Rev.* 63 (4), 1102–1116.
- Dobretsov, N.L.**, 2008. Geological implications of the thermochemical plume model. *Russ. Geol. Geophys.* 49 (7), 441–454, doi: 10.1016/j.rgg.2008.06.002.
- Dobretsov, N.L., Buslov, M.M.**, 2011. Problems of geodynamics, tectonics, and metallogeny of orogens. *Russ. Geol. Geophys.* 52 (12), 1505–1515, doi: 10.1016/j.rgg.2011.11.012.
- Dobretsov, N.L., Borisenko, A.S., Izokh, A.E., Zhmodik, S.M.**, 2010. A thermochemical model of Eurasian Permo-Triassic mantle plumes as a basis for prediction and exploration for Cu-Ni-PGE and rare-metal ore deposits. *Russ. Geol. Geophys.* 51 (9), 903–924, doi: 10.1016/j.rgg.2010.08.002.
- Dong, G.C., Mo, X.X., Zhao, Z.D., Zhu, D.C., Xie, X.F., Dong, M.L.**, 2011. The Neocene magmatism from Namuru intrusion in western Gangdese, Tibet and its tectonic significance. *Acta Petrolog. Sin.* 27 (7), 1983–1992.
- Dong, M.C., Zhao, Z.D., Zhu, D.C., Liu, D., Dong, G.C., Mo, X.X., Hu, Z.C., Liu, Y.S., Zou, Z.H.**, 2015. Geochronology, geochemistry, and petrogenesis of the intermediate and acid dykes in Linzhou Basin, southern Tibet. *Acta Petrolog. Sin.* 31 (5), 1268–1284.
- Fei, G.C., Zhao, F.M., Xu, J.B., Li, Y.G.**, 2014. Geochemical characteristics and its geological implications of Madeng volcanic rocks in Anduo, North Tibet. *J. Mineral. Petrol.* 34 (1), 46–51.
- Garzanti, E., Baud, A., Mascle, G.**, 1987. Sedimentary record of the northward flight of India and its collision with Eurasia (Ladakh Himalaya, India). *Geodin. Acta* 1 (4/5), 297–312.
- Guo, Z F., Wilson, M., Liu, J.Q.**, 2007. Post-collisional adakites in south Tibet: Products of partial melting of subduction-modified lower crust. *Lithos* 96, 205–224.
- Guo, Z F., Wilson, M., Zhang, M.L., Cheng, Z.H., Zhang, L.H.**, 2013. Post-collisional, K-rich mafic magmatism in south Tibet: Constraints on Indian slab-to-wedge transport processes and plateau uplift. *Contrib. Mineral. Petrol.* 165, 1311–1340.
- Hofmann, A.W.**, 1988. Chemical differentiation of the Earth: The relationship between mantle, continental crust, and oceanic crust. *Earth Planet. Sci. Lett.*, 90 (3), 297–314.
- Hoskin, P.W.O., Schaltegger, U.**, 2003. The composition of zircon and igneous and metamorphic petrogenesis, in: Manchar, J.M., Hoskin, P.W.O. (Eds.), *Zircon: Reviews of Mineralogy and Geochemistry*, Vol. 53, pp. 27–62.

- Hou, K.J., Li, Y.H., Zou, T.R., Qu, X.M., Shi, Y.R., Xie, G.Q.**, 2007. Laser ablation-MC-ICP-MS technique for Hf isotope microanalysis of zircon and its geological applications. *Acta Petrolog. Sin.* 23 (10), 2595–2604.
- Hou, Z.Q., Wang, E.Q., Mo, X.X., Ding, L., Pan, G.T., Zhang, Z.J.**, 2008. Collisional Orogeny and Metallogenesis of the Tibetan Plateau. Geol. Publ. House, Beijing.
- Hou, Z., Duan, L., Lu, Y., Zheng, Y., Zhu, D., Yang, Z., Wang, B., Pei, Y., Zhao, Z.**, 2015. Lithospheric architecture of the Lhasa Terrane and its control on ore 492 deposits in the Himalay-Tibetan Orogen. *Econ. Geol.* 110 (6), 1541–1575.
- Hu, X., Ma, R., Tao, X., Liu, D., Shi, H.**, 2007. Lithogeochemical characteristics and tectonic setting of volcanic rocks of Dianzhong Formation in the Coqen area, Tibet, China. *J. Chengdu Univ. Technol. (Sci. Technol. Ed.)* 33 (1), 15–21.
- Hu, X.M., Garzanti, E., Wang, J.G., Huang, W.T., An, W., Webb, A.**, 2016. The timing of India-Asia collision onset: Facts, theories, controversies. *Earth Sci. Rev.* 160, 264–299.
- Ji, W.Q., Wu, F.Y., Chung, S.L., Li, J.X., Liu, C.Z.**, 2009a. Zircon U-Pb geochronology and Hf isotopic constraints on petrogenesis of the Gangdese batholith, southern Tibet. *Chem. Geol.* 262, 229–245.
- Ji, W.Q., Wu, F.Y., Chung, S.L., Liu, C.Z.**, 2009b. Geochronology and petrogenesis of granitic rocks in Gangdese batholith, southern Tibet. *Sci. China (Ser. D)* 52 (9), 1240–1261.
- Ji, W.Q., Wu, F.Y., Liu, C.Z., Chung, S.L.**, 2012. Early Eocene crustal thickening in southern Tibet: New age and geochemical constraints from the Gangdese batholith. *J. Asian Earth Sci.* 53, 82–95.
- Jiang, J.S.** 2018. Genesis of Polymetallic Deposits and Prospecting Potential in the Linzizong Area, Western Gangdese Belt, Tibet Dissertation. China University of Geosciences, Beijing.
- Johnson, K.T.M., Dick, H.J.B., Shimizu, N.**, 1990. Melting in the oceanic upper mantle: An ion micro-probe study of diopsides in abyssal peridotites. *J. Geophys. Res. B.: Solid Earth*, 95 (B3), 2661–2678.
- Kaygusuz, A., Siebel, W., Sen, C.**, 2008. Petrochemistry and petrology of I-type granitoids in an arc setting: The composite Torul Pluton, Eastern Pontides, NE Turkey. *International J. Earth Sci.* 97 (4), 739–764.
- Kemp, A.I.S., Hawkesworth, C.J., Foster, G.L., Paterson, B.A., Woodhead, J.D., Hergt, J.M., Gray, C.M., Whitehouse, M.J.**, 2007. Magmatic and crustal differentiation history of granitic rocks from Hf-O isotopes in zircon. *Science* 315 (5814), 980–983.
- Khromykh, S.V., Vladimirov, A.G., Izokh, A.E., Travin, A.V., Prokop'ev, I.R., Azimbaev, E., Lobanov, S.S.**, 2013. Petrology and geochemistry of gabbro and picrites from the Altai collisional system of Hercynides: evidence for the activity of the Tarim plume. *Russ. Geol. Geophys.* 54 (10), 1288–1304, doi: 10.1016/j.rgg.2013.09.011.
- Kieffer, B., Arndt, N., Lapierre, H., Bastien, F., Bosch, D.C.**, 2004. Flood and shield basalts from Ethiopia: Magmas from the African superswell. *J. Petrol.* 45 (4), 793–834.
- Le Maitre, R.W.**, 2002. Igneous Rocks: A Classification and Glossary of Terms. Cambridge University Press, Cambridge, pp. 33–39.
- Li, C.**, 1987. The Longmucuo-Shuanghu-Lancangjiang plate suture and the north boundary of distribution of Gondwana facies Permo-Carboniferous system in northern Xizang, China. *J. Changchun College Geol.* 17 (2), 155–166.
- Li, F., Liu, W., Zhang, S., Wang, B.**, 2012. LA-ICP-MS zircon U-Pb dating and geochemical characteristics of Zhula intrusion in eastern Gangdese, Tibet. *Geol. Bull. China*, 31 (9), 1420–1434.
- Liu, Y.G., Li, W.Y., Jia, Q.Z., Zhang, Z.W., Wang, Z.A., Zhang, Z.B., Zhang, J.W., Qian, B.**, 2018. The dynamic sulfide saturation process and a possible slab break-off model for the giant Xiarihamu magmatic nickel ore deposit in the East Kunlun orogenic belt, Northern Qinghai-Tibet Plateau, China. *Econ. Geol.* 113 (6), 1383–1417.
- Liu, Y.G., Chen, Z.G., Li, W.Y., Xu, X.H., Kou, X., Jia, Q.Z., Zhang, Z.W., Liu, F., Wang, Y.L., You, M.X.**, 2019. The Cu-Ni mineralization potential of the Kaimuqi mafic-ultramafic complex and the indicators for the magmatic Cu-Ni sulfide deposit exploration in the East Kunlun Orogenic Belt, Northern Qinghai-Tibet Plateau, China. *J. Geochem. Explor.* 198, 41–53.
- Lü, B.X., Wang, Z., Zhang, N.D., Duan, J.Z., Gao, ZY., Shen, GF., Pan, CY., Yao, P.**, 1993. Granitoids in the Sanjiang Region (Nujiang-Lancangjiang-Jinshajiang Region) and Their Metallogenic Specialization. Geol. Publ. House, Beijing, pp. 169–243.
- Lü Xin, Wang Zhenghua, Liu Yulin, Liu Hongfei, Xu Kaifeng, Zhang Jinshu**, 2015. Geochronology and geochemistry of the Late Cretaceous to Paleocene intrusions in East Gangdese, Lhasa, Tibet and their tectonic significances. *Acta Geol. Sin.* 89 (2), 441–466.
- McCarron, J.J., Smellie, J.L.**, 1998. Tectonic implications of fore-arc magmatism and generation of high magnesian andesites: Alexander Island, Antarctica. *J. Geol. Soc.* 155 (2), 269–280.

Mo, X.X., Pan, G.T., 2006. From the Tethys to the formation of the Qinghai-Tibet Plateau: constrained by tectono-magmatic events. *Earth Sci. Front.* 13 (6), 795–803.

Mo, X.X., Dong, G.C., Zhao, Z.D., Guo, T.Y., Wang, L.L., Chen, T., 2005. Timing of magma mixing in the Gangdisê magmatic belt during the India-Asia collision: Zircon SHRIMP U-Pb dating. *Acta Geol. Sin.* 79 (1), 66–76.

Mo, X.X., Zhao, Z.D., Zhou, S., Dong, G.C., Liao, Z.L., 2007a. On the timing of India-Asia continental collision. *Geol. Bull. China* 26 (10), 1240–1244.

Mo, X.X., Hou, Z.Q., Niu, Y.L., Dong, G.C., Qu, X.M., Zhao, Z.D., Yang, Z.M., 2007b. Mantle contributions to crustal thickening during continental collision: Evidence from Cenozoic igneous rocks in southern Tibet. *Lithos* 96 (1–2), 225–242.

Mo, X.X., Niu, Y.L., Dong, G.C., Zhao, Z.D., Hou, Z.Q., Zhou, S., Ke, S., 2008. Contribution of syncollisional felsic magmatism to continental crust growth: A case study of the Paleogene Linzizong volcanic succession in southern Tibet. *Chem. Geol.* 250 (1–4), 49–67.

Mo, X.X., Zhao, Z.D., Yu, X.H., Dong, G.C., Li, Y.G., Zhou, S., Liao, Z.L., Zhu, D.C., 2009. Cenozoic Collisional-Postcollisional Igneous Rocks in the Tibetan Plateau. Geol. Publ. House, Beijing, pp. 1–396.

Pan, G.T., Mo, X.X., Hou, Z.Q., Zhu, D.C., Wang, L.Q., Li, G.M., Zhao, Z.D., Geng, Q.R., Liao, Z.L., 2006. Spatial-temporal framework of the Gangdese orogenic belt and its evolution. *Acta Petrolog. Sin.* 22 (3), 521–533.

Pearce, J.A., Harris, N.B.W., Tindle, A.G., 1984. Trace element discrimination diagram for the tectonic interpretation of granitic rocks. *J. Petrol.* 25 (4), 956–983.

Ponomarchuk, V.A., Dobretsov, N.L., Lazareva, E.V., Zhmodik, S.M., Karmanov, N.S., Tols-tov, A.V., Pyryaev, A.N., 2020. Evidence of microbial-induced mineralization in rocks of the Tomtor carbonatite complex (Arctic Siberia). *Dokl. Earth Sci.* 490, 76–80.

Rapp, R.P., 1997. Heterogeneous source regions for Archean granitoids: experimental and geochemical evidence, in: de Wit, M.J., Ashwal, L.D. (Eds.), Greenstone Belts. Oxford Monographs on Geology and Geophysics, Vol. 35, pp. 267–279.

Rickwood, P.C., 1989. Boundary lines within petrologic diagrams which use oxides of major and minor elements. *Lithos*, 22 (4), 247–263.

Rollinson, H.R., 1993. Using Geochemical Data: Evaluation, Presentation, Interpretation. Longman, London.

Rowley, D.B., 1996. Age of initiation of collision between India and Asia: a review of stratigraphic data. *Earth Planet. Sci. Lett.* 145, 1–13.

Rowley, D.B., 1998. Minimum age of initiation of collision between India and Asia north of the Everest based on the subsidence history of the Zhepure Mountain section. *J. Geol.* 106, 229–235.

Searle, M.P., Windley, B.F., Coward, M.P., Cooper, D.J.W., Rex, A.J., Rex, D., Li, T.D., Xiao, X.C., Jan, M.Q., Thakur, V., Kumar, S., 1987. The closing of Tethys and the tectonics of the Himalaya. *GSA Bull.* 98 (6), 678–701.

Schmidberger, S.S., Hegner, E., 1999. Geochemistry and isotope systematics of calc-alkaline volcanic rocks from the Saar-Nahe basin (SW Germany): Implications for Late-Variscan orogenic development. *Contrib. Mineral. Petrol.* 135 (4), 373–385.

Song, B., 2015. SHRIMP zircon U-Pb age measurement: Sample preparation, measurement, data processing and explanation. *Geol. Bull. China* 34 (10), 1777–1788.

Stupak, F.M., Yarmolyuk, V.V., Kudryashova, E.A., 2020. Late Mesozoic volcanism in the Ust'-Kara basin (eastern Transbaikalia) and its relationship with magmatism of the great Xing'An and East Mongolian volcanic belts. *Russ. Geol. Geophys.* 61 (1), 14–25, doi: 10.15372/RGG2019113.

Sun, S.S., McDonough, W.F., 1989. Chemical and isotope systematics of oceanic basalts: Implications for mantle composition and processes, in: Saunders, A.D., Norry, M.J. (Eds.), Magmatism in Ocean Basins. *Geol. Soc. London, Spec. Publ.* 42 (1), 313–345.

Sun, X., Zheng, Y.Y., Xu, J., Huang, L.H., Guo, F., Gao, S.B., 2017. Metallogenesis and ore controls of Cenozoic porphyry Mo deposits in the Gangdese Belt of southern Tibet. *Ore Geol. Rev.* 81, 996–1014.

Tang, J.X., Lang, X.H., Xie, F.W., Gao, Y.M., Li, Z.J., Huang, Y., Ding, F., Yang, H.H., Zhang, L., Wang, Q., Zhou, Y., 2015. Geological characteristics and genesis of the Jurassic No. I porphyry Cu-Au deposit in the Xiongcun district, Gangdese porphyry copper belt, Tibet. *Ore Geol. Rev.* 70, 438–456.

Taylor, S.R., McLennan, S.M., 1985. The Continental Crust: Its Composition and Evolution. Blackwell, Oxford, pp. 1–132.

Wang, C.S., Ding, X.L., 2003. The new researching progress of Tibet plateau uplift. *Adv. Earth Sci.* 13 (6), 526–532.

Wang, H.T., Zeng, L.S., Gao, L.E., Hu, Z.P., Wang, Y.F., Zhao, L.H., Gao, J.H., Xu, Q., 2019. Timing and geochemical characteristics of the Riduo granitic pluton within the Gangdese batholith, southern Tibet. *Acta Petrolog. Sin.* 35 (2), 439–454.

Wang, L.Q., Zhu, D.C., Geng, Q.R., Liao, Z.L., Pan, G.T., 2006. The age and significance of the granite porphyry related to collision in Linzhou basin of Gangdese, Tibet. *Chin. Sci. Bull.* 51 (16), 1920–1928.

Wang, R., Richards, J.P., Hou, Z.Q., An, F., Creaser, R.A., 2015. Zircon U–Pb age and Sr–Nd–Hf–O isotope geochemistry of the Paleocene–Eocene igneous rocks in western Gangdese: Evidence for the timing of Neo-Tethyan slab breakoff. *Lithos* 224–225, 179–194.

Wang, T., Wang, X.X., Guo, L., Zhang, L., Tong, Y., Li, S., Huang, H., Zhang, J.J., 2017. Granitoid and tectonics [in Chinese with English abstract]. *Acta Petrolog. Sin.* 33 (5), 1459–1478.

Wen, D.R., Liu, D.Y., Chung, S.L., Chu, M.F., Ji, J.Q., Zhang, Q., Song, B., Lee, T.Y., Yeh, M.W., Lo, C.H., 2008. Zircon SHRIMP U–Pb ages of the Gangdese batholith and implications for Neotethyan subduction in southern Tibet. *Chem. Geol.* 252 (3–4), 191–201.

Whalen, J.B., Currie, K.L., Chappell, B.W., 1987. A-type granites: Geochemical characteristics, discrimination and petrogenesis. *Contrib. Mineral. Petrol.* 95 (4), 407–419.

Wiedenbeck, M., Alle, P., Corfu, F., et al. Griffin, W.L., Meier, M., Oberli, F., von Quadt, A., Roddick, J.C., Spiegel, W., 1995. Three natural zircon standards for U–Th–Pb, Lu–Hf, trace element and REE analyses. *Geostand. Geoanalyt. Res.*, 19, 1–23.

Wilson, M., 2001. Igneous Petrogenesis. Kluwer Academic Publishers, London.

Wu, F.Y., Jahn, B.M., Wilde, S.A., Lo, C.-H., Yui, T.-F., Lin, Q., Ge, W.-C., Sun, D.-Y., 2003. Highly fractionated I-type granites in NE China (I): geochronology and petrogenesis. *Lithos* 66 (3–4), 241–273.

Wu, F.Y., Li, X.H., Zheng, Y.F., Gao, S., 2007. Lu–Hf isotopic systematics and their applications in petrology. *Acta Petrolog. Sin.* 23 (2), 185–220.

Wu, Y.B., Zheng, Y.F., 2004. Genesis of zircon and its constraints on interpretation of U–Pb age. *Chin. Sci. Bull.* 49 (15), 1554–1569.

Xie, B.J., Zhou, S., Xie, G.G., Tian, M.Z., Liao, Z.L., 2013a. Zircon SHRIMP U–Pb data and regional contrasts of geochemical characteristics of Linzizong volcanic rocks from Konglong and Dinrenle region, middle Gangdese Belt. *Acta Petrolog. Sin.* 29 (11), 3803–3814.

Xie, J.C., Li, W.K., Dong, G.C., Mo, X.X., Zhao, Z.D., Yu, J.C., Wang, T.C., 2013b. Petrology, geochemistry and tectonic significance of the granites from Basu area, Tibet. *Acta Petrolog. Sin.* 29 (11), 3779–3791.

Xu, W.C., 2010. Spatial variation of zircon U–Pb ages and Hf isotopic compositions of the Gangdese granitoids and its geologic implications. PhD Dissertation. China Univ. Geosci., Wuhan, pp. 1–96.

Yan, J.J., Zhao, Z.D., Liu, D., Wang, Z.Z., Tang, Y., 2017. Geochemistry and petrogenesis of the Late Jurassic Xuru Tso batholith in central Lhasa Terrane, Tibet. *Acta Petrolog. Sin.* 33 (8), 2437–2453.

Yin, A., Harrison, T.M., 2000. Geologic evolution of the Himalayan–Tibetan orogen. *Annu. Rev. Earth Planet. Sci.* 28 (1), 211–280.

Yu, F., Li, Z.G., Zhao, Z.D., Xie, G.G., Dong, G.C., Zhou, S., Zhu, D.C., Mo, X.X., 2010. Geochemistry and implication of the Linzizong volcanic succession in Cuomai area, central-western Gangdese, Tibet. *Acta Petrolog. Sin.* 26 (7), 2217–2225.

Zhang, L.L., Zhu, D.C., Zhao, Z.D., Liao, Z.L., Wang, L.Q., Mo, X.X., 2011. Early Cretaceous granitoids in Xainza, Tibet: Evidence of slab break-off. *Acta Petrolog. Sin.* 27 (7), 1938–1948.

Zhang, X.Q., Zhu, D.C., Zhao, Z.D., Sui, Q.L., Wang, Q., Yuan, S.H., Hu, Z.C., Mo, X.X., 2012. Geochemistry, zircon U–Pb geochronology and in-situ Hf isotope of the Maiga batholith in Coqen, Tibet: Constraints on the petrogenesis of the Early Cretaceous granitoids in the central Lhasa Terrane. *Acta Petrolog. Sin.* 28 (5), 1615–1634.

Zhang, Z., Dong, X., Geng, G., Wang, W., Yu, F., Liu, F., 2010. Precambrian metamorphism of the northern Lhasa terrane, south Tibet and its tectonic implications. *Acta Geol. Sin.* 84 (4), 449–456.

Zhang, Z.M., Dong, X., Xiang, H., Liou, J.G., Santosh, M., 2013. Building of the deep Gangdese arc, South Tibet: Paleocene plutonism and granulite-facies metamorphism. *J. Petrol.* 54, 2547–2580.

Zhang, Z.M., Ding, L., Zhao, Z.D., Santosh, M., 2017. Tectonic evolution and dynamics of the Tibetan Plateau. *Gondwana Res.* 41, 1–8.

Zheng, Y.C., Hou, Z.Q., Gong, Y.L., Liang, W., Sun, Q.-J., Zhang, S., Fu, Q., Huang, K.-X., Li, Q.-Y., Li, W., 2014. Petrogenesis of Cretaceous adakite-like intrusions of the Gangdese plutonic belt, southern Tibet: implication for mid-ocean ridge subduction and crustal growth. *Lithos* 190–191, 240–263.

Zheng, K., Wu, C.L., Wei, C.J., Gao, Y.H., Guo, W.F., Chen, H.J., Wu, D., Gao, D., 2019. Geochemistry, zircon U–Pb geochronology and Hf isotopic characteristics for syenogranite and diorite from the western segment of North Altyn. *Acta Petrolog. Sin.* 35 (2), 541–557.

Zhu, D.C., Mo, X.X., Niu, Y.L., Zhao, Z.D., Wang, L.Q., Liu, Y.S., Wu, F.Y., 2009. Geochemical investigation of Early Cretaceous igneous rocks along an east-west traverse throughout the central Lhasa Terrane, Tibet. *Chem. Geol.* 268, 298–312.

Zhu, D.C., Zhao, Z.D., Niu, Y.L., Mo, X.X., Chung, S.L., Hou, Z.Q., Wang, L.Q., Wu, F.Y., 2011. The Lhasa terrane: Record of a microcontinent and its histories of drift and growth. *Earth Planet. Sci. Lett.* 301, 241–255.

Zhu, D.C., Zhao, Z.D., Niu, Y.L., Dilek, Y., Hou, Z.Q., Mo, X.X., 2013. The origin and pre-Cenozoic evolution of the Tibetan Plateau. *Gondwana Res.* 23 (4), 1429–1454.

Рекомендована
Н.Л. Добрецовым

Поступила в редакцию 16 сентября 2019 г.
принята в печать 31 августа 2020 г.